



City Research Online

City, University of London Institutional Repository

Citation: Omidyeganeh, M., Piomelli, U., Christensen, K.T. & Best, J.L. (2013). Large eddy simulation of interacting barchan dunes in a steady, unidirectional flow. JOURNAL OF GEOPHYSICAL RESEARCH-EARTH SURFACE, 118(4), pp. 2089-2104. doi: 10.1002/jgrf.20149

This is the accepted version of the paper.

This version of the publication may differ from the final published version.

Permanent repository link: <https://openaccess.city.ac.uk/id/eprint/6943/>

Link to published version: <https://doi.org/10.1002/jgrf.20149>

Copyright: City Research Online aims to make research outputs of City, University of London available to a wider audience. Copyright and Moral Rights remain with the author(s) and/or copyright holders. URLs from City Research Online may be freely distributed and linked to.

Reuse: Copies of full items can be used for personal research or study, educational, or not-for-profit purposes without prior permission or charge. Provided that the authors, title and full bibliographic details are credited, a hyperlink and/or URL is given for the original metadata page and the content is not changed in any way.

City Research Online:

<http://openaccess.city.ac.uk/>

publications@city.ac.uk

1 Large-eddy simulation of interacting barchan dunes
2 in a steady, unidirectional flow.

Mohammad Omidyeganeh,¹ Ugo Piomelli,¹ Kenneth T. Christensen,² and

James L. Best^{2,3}

¹Department of Mechanical Engineering
and Materials, Queen's University,
Kingston, Ontario, Canada.

²Department of Mechanical Science and
Engineering, University of Illinois,
Urbana-Champaign, Illinois, USA.

³Departments of Geology, Geography and
Geographic Information Science and Ven Te
Chow Hydrosystems Laboratory, University
of Illinois, Urbana-Champaign, Illinois,
USA.

3 **Abstract.** We have performed large-eddy simulations of turbulent flow
4 over barchan dunes in a channel with different interdune spacings in the down-
5 stream direction at Reynolds number, $Re_\infty \simeq 26000$ (based on the free
6 stream velocity and channel height). Simulations are validated against ex-
7 perimental data (at $Re_\infty = 55460$); the largest interdune spacing (2.38λ ,
8 where λ is the length of the barchan model) presents similar characteristics
9 to the isolated dune in the experiment, indicating that at this distance the
10 sheltering effect of the upstream dune is rather weak. We examine 3D real-
11 izations of the mean and instantaneous flow to explain features of the flow
12 field relevant to sediment transport. Barchan dunes induce two counter-rotating
13 streamwise vortices, along each of the horns, which direct high-momentum
14 fluid toward the symmetry plane and low-momentum fluid near the bed away
15 from the centerline. The flow near the bed, upstream of the dune, diverges
16 from the centerline plane, decelerates and then rises on the stoss side of the
17 dune while accelerating; the flow close to the centerline plane separates at
18 the crest and reattaches on the bed. Away from the centerline plane and along
19 the horns, flow separation occurs intermittently. The flow in the separation
20 bubble is routed towards the horns and leaves the dune at their tips. The
21 separated flow at the crest reattaches on the bed, except on the centerline
22 symmetry plane of the dune, where a weak saddle point of separation ap-
23 pears at the bed. The distribution of the bed shear-stress, characteristics of
24 the separation and reattachment regions, and instantaneous wall turbulence
25 are discussed. Characteristics of the internal boundary layer developing on

26 the bed after the reattachment region are studied. The interdune spacing is
27 found to affect significantly the turbulent flow over the stoss side of the down-
28 stream dunes; at smaller interdune-spacings, coherent high- and low- speed
29 streaks are shorter but stronger, and the spanwise normal Reynolds stress
30 is larger. The turbulent kinetic energy budgets show the importance of the
31 pressure transport and mean-flow advection in transporting energy from the
32 overlying wake layer to the internal boundary layer over the stoss side of the
33 closely-spaced dunes. The characteristics of the separated-shear layer are al-
34 tered slightly at smaller interdune spacing; the separation bubble is smaller,
35 the separated-shear layer is stronger, and the bed shear-stress is larger. Away
36 from the dunes, typical wall-turbulence structures are observed, but coher-
37 ent eddies generated in the separated-shear layer due to the Kelvin-Helmholtz
38 instability are dominant near the dune. Coherent structures are generated
39 more frequently at smaller interdune spacing; they move farther away from
40 the bed, towards the free surface, and remain in between the horns. At larger
41 interdune spacings, these coherent structures are advected in the spanwise
42 direction with the mean streamwise vortices and can be observed outside of
43 the dunes.

1. Introduction

44 The interaction of turbulent flow with a mobile sand bed, when the flow is unidirectional
45 and sand supply is limited, results in the formation of barchan dunes in aeolian, marine
46 and fluvial environments. Barchans have a planform crescentic topography with horns
47 elongated in the downstream direction [*Kroy et al.*, 2005], and are extensively observed
48 in deserts on Earth [*Bagnold*, 1941; *Lancaster*, 1995], and on Mars [*Breed et al.*, 1979],
49 but more rarely in rivers and the oceans [*McCullogh and Janda*, 1964; *Allen*, 1968]. The
50 linear relationship between the width of the dune, its height and wavelength and its three-
51 dimensional shape are well understood [*Hesp and Hastings*, 1998]. Barchans rarely exist
52 as isolated forms and may occur in large fields [*Hersen et al.*, 2004] up to several hundred
53 square kilometers in area [*Lettau and Lettau*, 1969]. The sediment transport associated
54 with barchan dunes has attracted many researchers to study their fluid and morphological
55 dynamics in many differing environments with barchans.

56 The complexity of the three-way coupling between bedform, fluid flow, and sediment
57 transport can be simplified by considering one or two of these mechanisms in isolation
58 and then extracting their influence on the others [*Best*, 2005]. This simplification is
59 justified knowing that sediment transport occurs at smaller spatio-temporal scales than
60 the energetic flow scales, and that these are smaller than the scales of bedform deformation
61 and interaction [*Hersen et al.*, 2004].

62 After the early work by *Bagnold* [1941], the geomorphology of sand dunes has been stud-
63 ied and discussed in review papers by *Andreotti et al.* [2002] and *Livingstone et al.* [2007].
64 A body of research has been devoted to small-scale grain transport mechanisms over

65 flat surfaces [*Andreotti et al.*, 2002] and sloping bedforms considering the changes in the
66 threshold of sediment transport [*Hardisty and Whitehouse*, 1988; *Iversen and Rasmussen*,
67 1994]. Other research has studied the large-scale dynamics of dunes by examining their
68 dimensions [*Hesp and Hastings*, 1998] and interactions within dune fields [*Breed et al.*,
69 1979], both experimentally [*Endo et al.*, 2004], or by modelling sand transport in a large
70 domain and predicting an equilibrium state for their size and arrangement [*Lima et al.*,
71 2002].

72 Models for solitary dunes cannot describe the steady state of barchan dune fields [*Hersen*
73 *et al.*, 2004]; dunes receive sediment on their stoss side, and lose sediment through their
74 horns; hence large dunes grow and move slowly while small dunes shrink and move faster.
75 Additionally, based on the models in literature, the length scales required for the instability
76 of deformation are much smaller than the dune sizes found in nature [*Hersen et al.*, 2004];
77 hence, there must be yet unknown physics that keep dune fields steady and determine the
78 interdune spacing.

79 Most measurements and calculations of flow and sediment transport have been per-
80 formed on the streamwise-wall-normal symmetry plane of barchans, especially over the
81 windward stoss side [*Lancaster*, 1985; *Walmsley and Howard*, 1985; *Lancaster et al.*, 1996;
82 *Wiggs et al.*, 1996; *McKenna Neuman et al.*, 2000; *Palmer et al.*, 2012]. Theoretical efforts
83 have also usually considered transverse dunes [*Lancaster*, 1985; *Walmsley and Howard*,
84 1985; *Frank and Kocurek*, 1996; *Lancaster et al.*, 1996; *Wiggs et al.*, 1996; *McKenna Neu-*
85 *man et al.*, 2000] and adapted an extended version of boundary layer theory [*Schlichting*,
86 1955] to the flow over gently sloping symmetrical hills [*Jackson and Hunt*, 1975]. However,
87 the velocity profiles do not often obey the logarithmic law-of-the-wall over barchan dunes

88 [*Frank and Kocurek, 1996; Wiggs et al., 1996; McKenna Neuman et al., 2000*]. Early nu-
89 merial experiments on the development and migration of an isolated dune by *Wippermann*
90 *and Gross* [1986] assumed log-linear behavior and could just explain the sensitivity of the
91 wind speed on the shape of barchan dunes, similar to the picture presented by *Bagnold*
92 [1941], *Finkel* [1959] and *Allen* [1968].

93 Advanced analysis of flow characteristics has often been performed over transverse dunes
94 [*Frank and Kocurek, 1996; McKenna Neuman et al., 2000*]. Some theoretical efforts [*Frank*
95 *and Kocurek, 1996*] explained the shear layers over the lee side of aeolian dunes and
96 development of a thin internal boundary layer downstream of the flow reattachment region.
97 The intermittent behavior of turbulence structures and sediment transport was studied by
98 *McKenna Neuman et al.* [2000] who studied the frequency spectra of streamwise velocity
99 fluctuations and sediment transport over trasverse dunes. At low wind speeds, close to
100 the sediment transport threshold, the intermittent nature of flow structures on sediment
101 transport was found to be as important as the mean flow. *McKenna Neuman et al.* [2000]
102 concluded that mean velocity is not a good indicator of sediment transport mechanisms
103 at low wind speeds. The secondary flow over the lee side of transverse dunes has been
104 studied by *Walker and Nickling* [2002, 2003]; grainfall transport and deposition is strongly
105 linked with the vertical flow within the shear layer bounding the circulation bubble in the
106 wake. The reversed flow in the recirculation cell was found to be strong enough to return
107 sediment to the lee side of the dune [*Walker and Nickling, 2003*].

108 An interesting and yet ambiguous phenomenon in the morphology of barchan and trans-
109 verse dunes is the sediment transport mechanism upstream of the toe of the dune, where
110 the mean bed shear-stress decreases but, contrary to the expectation of sediment depo-

111 sition in this area, the transport rate does not decrease. Researchers conjecture that
112 turbulence structures are responsible for sediment transport in this region [*Wiggs et al.*,
113 1996; *McKenna Neuman et al.*, 2000; *Walker and Nickling*, 2002, 2003; *Parsons et al.*,
114 2004a; *Weaver and Wiggs*, 2011]. The majority of sand transported is due to long-lasting
115 positive wind fluctuations, while the influence of short time-scale events on the sediment
116 transport is not yet understood. The concave curvature of streamlines was assumed to
117 be responsible for the increase in Reynolds shear stresses [*Wiggs et al.*, 1996], with high-
118 momentum structures being transferred to the low-momentum area near the bed, which
119 increases the instability and hence the stress.

120 On the upper half of the stoss side, the bedform curvature changes from concave to con-
121 vex, which stabilizes the flow that is also accelerated; these two mechanisms have opposing
122 effects on sediment transport, with acceleration often overcoming the effects of curvature
123 [*Weaver and Wiggs*, 2011]. A third zone exists if the dune crest does not coincide with the
124 brink; flow decelerates after the crest towards the brink that, together with the convex
125 curvature, cause deposition of sand [*Wiggs et al.*, 1996]. The dune profile (crest-brink
126 separated or crest-brink coincident) thus affects the lee side flow characteristics [*Baddock*
127 *et al.*, 2011]. While an increase in Reynolds shear stress and the streamwise component
128 of stress can explain the maintenance of sand flux at the toe, further downstream, on
129 the stoss side and near the crest, flow acceleration plays a more significant role [*Walker*
130 *and Nickling*, 2003; *Weaver and Wiggs*, 2011]. A more sophisticated study is required
131 to clarify the effects of acceleration and streamline curvature on the turbulence statistics
132 and their budgets.

133 Several numerical studies have been conducted concerning flow over three-dimensional
134 barchan dunes [*Wippermann and Gross, 1986; Takahashi et al., 1998*]; they generally suffer
135 from low grid resolution and inaccurate models. Reynolds-averaged Navier-Stokes solvers
136 in 2D [*Parsons et al., 2004a, b*] and 3D [*Hermann et al., 2005*] provide mean-flow char-
137 acteristics (flow acceleration/deceleration, separation, reattachment, and reversal) with
138 qualitative agreement with the literature, but neglect the mean-flow three-dimensionality
139 and do not provide information on the instantaneous flow structures observed in experi-
140 ments [*McKenna Neuman et al., 2000; Franklin and Charru, 2011*] and their importance;
141 e.g., elongated sand streaks observed on the stoss side of dunes, which indicate signifi-
142 cant contributions of wall turbulence to sediment transport [*Franklin and Charru, 2011;*
143 *Charru and Franklin, 2012*].

144 The effects of interdune spacing on dune dynamics have been largely ignored, despite the
145 fact that the spacing affects the flow on the lee side of the upstream dune and the stoss side
146 of the downstream bedform [*Fernandez et al., 2006*], and may change the mechanisms of
147 sediment transport, which are assumed to depend on the spacing and dune sizes [*Walker*
148 *and Nickling, 2003; Baddock et al., 2007; Palmer et al., 2012*]. The importance of the
149 secondary flows observed in the lee side on intermittent sediment transport over the stoss
150 side of the downstream dune was studied by *Walker and Nickling* [2003]; high variability
151 in bed shear-stress in the reattachment zone inhibits sediment deposition and can cause
152 deformation of the stoss side of the downstream dune. At interdune spacings close to
153 the size of the separation zone, regular deformation models [*McLean and Smith, 1986*]
154 cannot explain the physics, even for transverse dunes [*Baddock et al., 2007*]. *Palmer et al.*
155 [2012] conducted a series of novel experiments on the effects of interdune spacing on the

156 features of the separated shear-layer, separation-bubble size and approaching turbulence
157 structures on the stoss side of the downstream dune. The sheltering effect of the upstream
158 dune on the flow over the downstream dune, in which the vortices formed on the separation
159 zone shear layer were advected downstream and transported energy to smaller scales, was
160 identified.

161 The process of interaction between barchan dunes has been studied in aeolian [*Kocurek*
162 *et al.*, 2010] and aqueous [*Endo et al.*, 2004] environments. In water flows, *Endo et al.*
163 [2004] observed three types of interaction occurring as the volumetric ratio between the two
164 adjacent bedforms increased: (1) absorption, (2) ejection, and (3) splitting. *Kocurek et al.*
165 [2010] supported the hypothesis that interactions emerge from bedform-level sediment
166 transport in a hierarchy that includes grain-fluid interactions and dune-dune interactions.

167 However, all efforts to date lack an accurate representation of the bed shear-stress,
168 which provides insight on the sediment transport mechanisms in a three-dimensional view.
169 Turbulent flow over the lee side of the dune, where the flow separates at the crest and broad
170 ranges of length- and time-scales are introduced into the turbulence spectrum, is poorly
171 understood. This situation is even more complicated as the flow separates intermittently
172 on the horns of the dune and, on some parts of the crestline, it is oblique with respect
173 to the crestline. Additionally, the three-dimensional characteristics of mean flow and
174 turbulence have yet to be studied with a reasonable resolution. The significant effect of
175 interdune spacing on the mean-flow and instantaneous flow features have also yet to be
176 examined in detail. In this paper, we present a series of resolved large-eddy simulations
177 of flow over a model barchan dune similar to that studied experimentally by *Palmer et al.*
178 [2012] at various interdune spacings, to obtain a more comprehensive understanding of

179 the 3D mean flow characteristics and turbulence coherent structures at differing dune
180 spacings.

2. Problem formulation

181 In large-eddy simulations, the velocity field is separated into a resolved (large-scale)
182 and a subgrid (small-scale) field, by a spatial filtering operation [*Leonard, 1974*]. The
183 non-dimensionalized continuity and Navier-Stokes equations for the resolved velocity field
184 are

$$185 \quad \frac{\partial \bar{u}_i}{\partial x_i} = 0, \quad (1)$$

$$186 \quad \frac{\partial \bar{u}_i}{\partial t} + \frac{\partial \bar{u}_i \bar{u}_j}{\partial x_j} = -\frac{\partial \bar{P}}{\partial x_i} - \frac{\partial \tau_{ij}}{\partial x_j} + \frac{1}{Re_\infty} \nabla^2 \bar{u}_i + f_i \delta_{i,1}, \quad (2)$$

188 where $Re_\infty = U_\infty h / \nu$, h is the channel height, and U_∞ is the free-stream velocity over the
189 toe of the dune. We use U_∞ for the normalization of the statistics throughout the paper.
190 x_1 , x_2 and x_3 are the streamwise, vertical and spanwise directions, also referred to as x ,
191 y and z . The velocity components in these directions are, respectively, u_1 , u_2 and u_3 (or
192 u , v and w). An overline denotes a filtered quantity, and $\tau_{ij} = \overline{u_i u_j} - \bar{u}_i \bar{u}_j$ are the subgrid
193 stresses, which were modeled using an eddy-viscosity assumption

$$194 \quad \tau_{ij} - \delta_{ij} \tau_{kk} / 3 = -2\nu_T \bar{S}_{ij} = -2C \bar{\Delta}^2 |\bar{S}| \bar{S}_{ij}. \quad (3)$$

195 Here, $\bar{\Delta} = 2(\Delta x \Delta y \Delta z)^{1/3}$ is the filter size, $\bar{S}_{ij} = (\partial \bar{u}_i / \partial x_j + \partial \bar{u}_j / \partial x_i) / 2$ is the resolved
196 strain-rate tensor and $|\bar{S}| = (2\bar{S}_{ij} \bar{S}_{ij})^{1/2}$ is its magnitude. The coefficient C is determined
197 using the dynamic model [*Germano et al., 1991*] with the Lagrangian averaging technique
198 proposed by *Meneveau et al.* [1996], and extended to non-Cartesian geometries by *Jordan*
199 [1999] and *Armenio and Piomelli* [2000]. The flow is driven by a mean pressure gradient,
200 f_i , which is determined at each time step to ensure a fixed flow rate through the channel.

201 The governing differential equations (1) and (2) are discretized on a non-staggered grid
202 using a curvilinear finite-volume code. The method of *Rhie and Chow* [1983] is used
203 to avoid pressure oscillations. Both convective and diffusive fluxes are approximated
204 by second-order central differences. A second-order-accurate semi-implicit fractional-
205 step procedure [*Kim and Moin*, 1985] is used for the temporal discretization. The
206 Crank-Nicolson scheme is used for the wall-normal diffusive terms, and the Adams-
207 Bashforth scheme for all the other terms. Fourier transforms are used to reduce the
208 three-dimensional Poisson equation into a series of two-dimensional Helmholtz equations
209 in wave-number space, which are solved iteratively using the BiConjugate Gradient Sta-
210 bilized method. The code is parallelized using the Message-Passing Interface and the
211 domain-decomposition technique, which have been extensively tested for turbulent flows
212 [*Silva Lopes and Palma*, 2002; *Silva Lopes et al.*, 2006; *Radhakrishnan et al.*, 2006, 2008;
213 *Omidyeganeh and Piomelli*, 2011].

214 The barchan dune (Figure 1) was generated from the model used in the experiments of
215 *Palmer et al.* [2012] that reflects the typical shape of barchans in nature [*Hersen et al.*,
216 2004]. The aspect ratio of the current model falls in the range of laboratory and field
217 measurements [*Palmer et al.*, 2012]. The barchan model has a length of $\lambda = 3.62h$, width
218 of $W = 3.62h$, and height of $H = 0.135h$. The ratio of the dune height, H , to the channel
219 height, h , is equal to the ratio of the dune height to the boundary layer thickness in the
220 experiment [*Palmer et al.*, 2012]. The simulation adopts an immersed boundary method
221 based on the volume of fluid (VOF) technique [*Hirt and Nicholas*, 1981] to model the
222 barchan. On the bed, the no-slip boundary condition is used, and periodic boundary
223 conditions are employed in the streamwise (x) and spanwise (z) directions. The top

224 surface is assumed to be rigid and free of shear stress: the vertical velocity is set to zero
225 there, as are the vertical derivatives of the streamwise and spanwise velocity components.
226 The Reynolds number ranged between $25900 \leq Re_\infty \leq 26640$ for different simulations
227 and is less than half that of the experiments of *Palmer et al.* [2012] ($Re_\infty = 55460$).

228 A series of simulations was conducted to study the effects of interdune spacing on the
229 physics of the flow (Table 1). A Cartesian mesh was generated, with the grid distribution
230 in the wall-normal direction being uniform up to the highest point of the dune, and
231 then stretched by a hyperbolic tangent function. The grid in the spanwise direction was
232 uniform, while in the streamwise direction a higher resolution was used over the lee side of
233 the dunes, since the bed slope is significant in this zone and the flow separates. For all cases
234 mentioned in Table 1, the grid distribution was the same. We performed a grid refinement
235 study for Case 1 with a focus on the resolution of the VOF model over the lee side of
236 the dune, as well as the convergence of statistics. Three simulations with $64 \times 158 \times 128$,
237 $128 \times 158 \times 256$, and $160 \times 281 \times 512$ grid points were examined, with the two finest
238 simulations producing grid-converged results with resolution $\Delta x^+ < 28.86$, $\Delta y^+ < 0.83$,
239 and $\Delta z^+ < 10.55$, where the plus sign in the superscript represents normalization with
240 respect to the local bed shear-velocity u_τ and kinematic viscosity ν . First- and second-
241 order statistics were within 5% of each other for all resolutions. Only the results obtained
242 with the finest grid resolution are shown herein. Note that the grid spacings above are
243 comparable to those used in many Direct Numerical Simulations of the Navier-Stokes
244 equations.

245 The equations were integrated for $900H/U_\infty$ time units to remove transient effects, and
246 then statistics were accumulated over $1200H/U_\infty$ time units. To increase the sample size,

247 averaging was also performed over the symmetric points in the spanwise direction. To
248 verify the adequacy of the sample, we compared statistics obtained using only half of the
249 sample with those obtained using the complete sample, and found that the mean velocities
250 differed by less than 3%, and the root-mean-square (rms) intensities by less than 7%.

3. Results

251 The present model has been extensively validated in three-dimensional flows with sepa-
252 ration, [*Radhakrishnan et al.*, 2006, 2008], and over dunes in particular [*Omidyeganeh and*
253 *Piomelli*, 2011, 2013]. *Omidyeganeh and Piomelli* [2011] performed extensive quantitative
254 comparisons of the LES model (carried out with the present code and with similar pa-
255 rameters and grid spacings) with experiments and other simulations for the flow over 2D
256 dunes, obtaining excellent agreement with the reference data with grid spacings similar to
257 the present; the extension to 3D dunes [*Omidyeganeh and Piomelli*, 2013] showed that the
258 main features of the flow are also captured well for highly three-dimensional mean flows.
259 In the present work, comparison of the numerical model with the experiments [*Palmer*
260 *et al.*, 2012] is difficult because of substantial differences between experimental and numer-
261 ical configurations. First of all, the periodic condition in the horizontal directions used in
262 the present model implies that we simulate the fully developed flow over an infinite array
263 of dunes, uniformly distributed in the streamwise and spanwise directions. The experi-
264 ments [*Palmer et al.*, 2012], on the other hand, considered either an isolated dune, or two
265 barchans in tandem with zero streamwise spacing. Secondly, the experiment was carried
266 out in a boundary layer, while in the simulation, since periodic boundary conditions were
267 used, no boundary layer growth was allowed, and the top boundary of the domain was a
268 line of symmetry; the lack of entrainment (or detrainment) thus alters the acceleration (or

269 deceleration) that the mean flow experiences, and may also affect some turbulence quanti-
270 ties. Finally, and most importantly, the Reynolds number in the experiment is over twice
271 that of the numerical simulation. Since the number of grid points required by a resolved
272 LES scales with $Re^{37/14}$ [Choi and Moin, 2012], the extra computational cost required by
273 a calculation that matched the experiment would have made this study infeasible. Despite
274 these differences, the agreement is qualitatively and quantitatively good, as will be shown
275 below. In the following, we first compare the numerical results with the experimental data
276 that are available only for the symmetry plane; then, we stress the three-dimensional fea-
277 tures of the mean flow. Finally, we examine instantaneous flow visualizations to highlight
278 the effects of the dune configuration on the turbulence structure.

3.1. Statistics in the symmetry plane

279 Mean streamwise velocity contours and streamlines are shown for experiments [Palmer
280 *et al.*, 2012] and simulations in Figure 2. We chose Cases 1 and 5, which more closely
281 resemble the experimental configurations: Case 5, which has the largest interdune spacing
282 is found to be similar to the isolated dune case, while Case 1 is similar to the case in
283 which measurements were taken over the second dune in an array with zero streamwise
284 spacing. An important difference between experimental and numerical results is the higher
285 velocity observed over the crest in the simulations, compared to the experiments. Two
286 reasons contribute to this behavior: the additional blockage in the open channel (compared
287 with the boundary layer), and secondary flows that are observed in the simulation, and
288 which will be discussed later. The flow separates at the crest and reattaches on the
289 bed at $x_r/H \simeq 4.5 - 5.6$. The predicted reattachment length is slightly larger than in
290 the experiments, perhaps because of the higher velocity over the crest predicted by the

291 simulations. In the zero-spacing cases (Figure 2(*c,d*)), the reattachment length decreases
292 further (compared to the isolated dune case) because of the bed-ward motion upstream
293 of the dunes, reflected by the streamline curvature at $x/H < -8.0$.

294 A comparison of the Reynolds shear stress between simulations and experiments (Figure
295 3) reveals the contribution of the upstream dune on the flow over the downstream barchan
296 when the dunes are close to each other. Although the separated shear layer is stronger in
297 the simulations due to the higher speed (and velocity gradient, $\partial\langle\bar{u}\rangle/\partial y$), the extension
298 of the shear layer towards the downstream dune agrees with the experiment. We also
299 observe good agreement between the case with the largest spacing and the isolated dune
300 of the experiment, indicating that, by 2.38λ , the sheltering effect of the upstream dune
301 on the downstream barchan has become small.

302 Velocity and Reynolds stresses are also shown in Figure 4, in which profiles are compared
303 at three locations: upstream of the dune ($x/H = -9.0$), at the crest ($x/H = 0.0$), and
304 over the lee side of the dune ($x/H = 2.0$). The freestream velocity at the toe of the
305 dune is used for normalization of the data. The behavior of the velocity profiles is similar
306 to the experiments [*Palmer et al.*, 2012], despite some differences that can be attributed
307 to the Reynolds number (the experimental profiles being fuller for instance). For the
308 zero-spacing case, the effect of the upstream dune is reflected in a two-layer structure
309 of the mean velocity, in which the wake with higher momentum overlies the internal
310 boundary layer at the bed; this results in an inflectional velocity profile. The inherent
311 instability of the inflectional profile results in higher levels of plane turbulent kinetic
312 energy, $q_s^2 = (\langle u'u' \rangle + \langle v'v' \rangle)/2$, and primary Reynolds shear stress, $-\langle u'v' \rangle/U_\infty^2$. On the
313 other hand, the isolated case shows a single layer, similar to a boundary layer profile,

314 and also to the largest interdune-spacing LES (Case 5). The two-layer profiles are still
315 observed over the crest (Figure 4(b)) but have disappeared over the lee side (Figure 4(c)).

316 The profiles of Reynolds stresses also show good agreement with the experiments. Two
317 peaks in the vertical profile of the turbulent kinetic energy, Figures 4(e) and (f), for Case
318 1 represent two shear layers, with the overlying one being weaker. At the crest (Figure
319 4(e)), there is a near-bed peak representing the developing boundary layer on the stoss
320 side for both simulations, and a second peak at $y/H \simeq 2.0$ for the zero-spacing case due
321 to the upstream dune. Over the lee side (Figure 4(f)), the outer-layer peak can still
322 be observed at $y/H \simeq 2.5$, while all cases show significant turbulent kinetic energy in
323 the separated-shear layer. Upstream of the dunes, Figure 4(d), the internal boundary
324 layer on the bed has a single peak, while the zero-spacing case has a second (outer) one
325 due to the separated-shear layer coming from upstream. The primary Reynolds shear
326 stresses (Figures 4(g-i)) are also more significant in the separated-shear layer, compared
327 to the developing boundary layer; at the crest, the peak of the profiles near the bed has
328 disappeared due to the acceleration of flow on the stoss side, which dampens the turbulence
329 near the bed [Weaver and Wiggs, 2011]. This behavior will be examined further later.

330 After flow reattachment, the flow on the centerline exhibits a region in which the pres-
331 sure gradient is nearly zero; this zone extends, for Case 5, from $x/H \simeq -49.5$ to -14.0 ,
332 for a total length of $35.5H$. The velocity profiles in wall units on four vertical lines along
333 this region are shown in Figure 5. The profiles approach the log-law from below, and at
334 the end of the zero pressure gradient zone they show a region of logarithmic behavior.
335 The boundary-layer recovery is faster at the beginning of the zero-pressure region, and
336 becomes significantly slower from $x/H = -30.0$ to $x/H = -14$. Although the velocity

337 profile shows a region of equilibrium, the flow is still developing slowly after $x/H \simeq -35$;
338 hence the recovery of the flow is not complete with this inter-dune spacing. *Baddock et al.*
339 [2011] reported $17.23H$ as the recovery distance of a barchan dune based on the mean
340 velocity close to the bed. Although they examined the recovery of flow for an isolated
341 dune, their result is close to this simulation, $14.5H$. The recovery distance of flow for
342 transverse dunes, $x/H > 25$ [*Walker and Nickling, 2003; Dong et al., 2007*], and in fluvial
343 environments, $x/H \simeq 30 - 50$ [*McLean and Smith, 1986*] are much larger than the current
344 results. *Frank and Kocurek [1996]*, however, reported a much smaller distance, $x/H \simeq 8$,
345 for the flow recovery for closely spaced transverse dunes. In general, the recovery mech-
346 anism is affected by the upper wake layer over the boundary layer; the energy transfer
347 between these two layers may enhance internal boundary layer development. After the
348 zero-pressure gradient zone, the flow decelerates due to the adverse pressure gradient up-
349 stream of the toe, and deviates again from an equilibrium state; the velocity profile goes
350 above the law-of-the-wall (Figure 5) as the bed shear-stress decreases.

351 Development of the root-mean-square (RMS) velocity fluctuations and primary
352 Reynolds shear stress in Case 5 is shown in Figure 6. At the beginning of the zero-
353 pressure-gradient region, the signature of the overlying wake layer appears as an outer
354 layer peak in the profiles of u'_{rms} and $u'v'^+$. The profiles further downstream ($x/H = -30.0$
355 and -14.0) are similar to each other, and justify our conclusion that the development of
356 the internal boundary layer slows down after $14.5H$. Spanwise and wall-normal Reynolds
357 stresses do not show the two peaks typical of wall-bounded flows with wake interac-
358 tion [*Balachandar and Patel, 2005*], where v'^+ and w'^+ profiles are significantly affected
359 throughout the depth, and the level of stresses are significantly higher than that noted

360 in a smooth open channel flow. Profiles at the toe of the downstream dune, after a zone
361 of deceleration, shows a significant increase of turbulence level, consistent with many ob-
362 servations in the literature [*Wiggs et al.*, 1996; *Walker and Nickling*, 2002, 2003; *Parsons*
363 *et al.*, 2004a; *Weaver and Wiggs*, 2011]. The sustained sediment transport that occurs in
364 this region, despite a decrease in the bed shear-stress, is usually explained by this increase
365 in turbulence activity.

366 For smaller interdune spacings, the zero-pressure-gradient zone is much shorter; it is
367 $1.8H$ for Case 1, $6.7H$ for Case 2, $11.9H$ for Case 3, $17.2H$ for Case 4, and $35.5H$ for
368 Case 5. Figure 7 shows the velocity profiles in wall units at the end of the zero-pressure
369 gradient zone of the simulations, and shows the region of deceleration at the toe of the
370 downstream dune to start earlier for larger interdune spacings. The internal boundary
371 layer is still in significant development at a small interdune spacing, while the difference
372 between Cases 4 and 5 is small, especially if we consider the very large difference between
373 their interdune spacings, $24.58H$.

374 The effect of interdune spacing on the Reynolds stresses in the toe region of dunes
375 is shown in Figure 8. As the interdune spacing decreases, the streamwise velocity fluc-
376 tuations in the boundary layer decrease, but the wall-normal and spanwise fluctuations
377 increase at the same time as the second peak in u^+ increases; the Reynolds shear stress re-
378 mains unchanged close to the wall, while in the overlying layer the wake region is stronger
379 for smaller interdune spacings. The decrease in the internal boundary layer stresses is
380 related to a shorter development distance, and the increase in the wake layer stresses is
381 related to a shorter decay distance of the upstream separated shear layer. If turbulence
382 activity near the bed sustains sediment transport at the toe of the dune [*McKenna Neu-*

383 *man et al.*, 2000], then sediment transport in this region should decrease with decreasing
 384 interdune spacing; this may explain the bedform repulsion effects found in deserts [*Ew-*
 385 *ing and Kocurek*, 2010] and experiments [*Endo et al.*, 2004] in which, if the approaching
 386 upstream dune is close to a downstream one (less than one dune length), it absorbs the
 387 dune by halting sediment transport in the toe region. Our results also indicate that the
 388 sediment transport at the toe may be decreased for distances of this order.

389 The skin friction coefficient,

$$390 \quad C_f = \frac{\tau_w}{1/2\rho U_\infty^2}, \quad (4)$$

391 along the stoss side of dunes on the centerline symmetry plane is shown in Figure 9, where
 392 τ_w is the bed shear stress. The skin friction increases as the flow rises along the stoss side
 393 and reaches the crest at $x/H = -0.1$. The interdune spacing affects the friction coefficient
 394 at the toe, $x/H = -8.0$, which changes by about 30%, while along the stoss slope the
 395 difference between cases is small. With larger interdune spacings, the bed shear-stress is
 396 smaller, and any difference in sediment transport caused by the mean shear stress would
 397 likely not be significant. Note that the skin friction oscillates along the stoss side due to
 398 the waviness of the surface of the model; the skin friction has a minimum at $x/H = -7.6$
 399 where the deceleration is maximum and the stoss side of the dune starts. The second
 400 minimum in the skin friction occurs at $x/H = -5.0$ due to a local deceleration of flow
 401 caused by these surface waves.

402 Figure 10 shows turbulence statistics along a line $0.1H$ above the bed. Through most of
 403 the zero-pressure gradient region, this line lies in the buffer layer. All cases present similar
 404 profiles; two peaks are present at the dune toe and on the stoss side. The peak at the
 405 toe, $x/H \simeq -8.0$, corresponds to flow deceleration which enhances turbulence; the second

406 peak at $x/H \simeq -5.0$ corresponds to the location where the wall stress has local minima
 407 (Figure 9). Reynolds stresses decay in the accelerating-flow region on the stoss side, even
 408 without the normalization of stresses with the bed-shear stress. The Reynolds shear stress
 409 (Figure 10(d)) is negative at the dune toe, but changes sign in the acceleration region.
 410 *Baddock et al.* [2011] observed a similar behavior and related this to the curvature of the
 411 bed, which is highest there; hence the definition of quadrants is altered and a positive
 412 value of $u'v'$ does not mean that the turbulence activity is fundamentally altered. We
 413 examined this conclusion by rotating the co-ordinate frame into parallel- and normal-to-
 414 bed co-ordinates; the rotation is a maximum at $x/H \simeq -5.0$ and is about 11° with respect
 415 to x . The Reynolds shear stress shown for Cases 2 and 4 in Figure 11 is negative in the
 416 new system of co-ordinates; the peak at $x/H = -5.0$ disappears when the stress is not
 417 normalized with the wall-shear stress and in general $\langle u'v' \rangle / U_\infty^2$ increases slightly over the
 418 stoss side due to acceleration.

419 At the dune toe, where the stoss side begins, the streamwise velocity fluctuations (Figure
 420 10(a)) are higher for Cases 4 and 5 (larger interdune spacing) by over 30%. The wall-
 421 normal and spanwise turbulence intensities, on the other hand, are significantly larger
 422 for small interdune spacings (Cases 1 and 2); the large differences in the intensities are
 423 consistent along the stoss side, and are not a local effect. We conjecture that penetration
 424 of the wake layer into the internal boundary layer at small interdune spacing causes a
 425 boost in the wall-normal and spanwise intensities all along the stoss side. We examined
 426 the budgets of the normal Reynolds stresses to understand the contribution of the wake
 427 layer to the turbulence intensities over the stoss side of dunes; significant differences exist
 428 between Cases 1 and 5 in $-\langle \bar{u} \rangle \partial \langle v'v' \rangle / \partial x$ and $-\langle w' \partial p' / \partial z \rangle / \rho$ that are dominant terms in

429 the mean-flow advection and the pressure transport of the wall-normal Reynolds stress,
 430 $\langle v'v' \rangle$, and the spanwise normal Reynolds stress, $\langle w'w' \rangle$, budgets respectively; these terms
 431 are larger in Case 1 by a factor greater than two.

432 At the dune toe, interdune spacings smaller than 1.02λ do not allow the wall turbulence
 433 to be amplified as the flow decelerates. Over the stoss side, the wake region overlying the
 434 internal boundary layer interacts with the wall region and enhances the wall-normal and
 435 spanwise turbulence in the cases with interdune spacings smaller than 0.68λ . Additionally,
 436 over the second half of the stoss side, the flow accelerates, which decreases the turbulence,
 437 but increases the skin friction. These modifications of the turbulence characteristics can
 438 be expected to affect significantly the sediment transport.

439 The flow separation at the crest produces a strong shear layer, which destabilizes the
 440 flow and increases turbulence. The Reynolds shear stress contours, shown in Figure 3,
 441 already highlight its importance. Velocity, turbulent kinetic energy, and Reynolds shear
 442 stress profiles along three vertical lines passing through the separated-shear layer are
 443 shown in Figure 12. $\langle v'v' \rangle/U_\infty^2$ and $\langle u'v' \rangle/U_\infty^2$ are significant in the shear layer where the
 444 mean flow bends towards the bed; $\langle w'w' \rangle/U_\infty^2$ presents significant turbulence in the shear
 445 layer and near the bed around the reattachment point. Profiles at $x/H = 2.0$, inside
 446 the separation bubble, show the reversed flow near the bed and the shear layer above it.
 447 The mean velocity in the separation bubble does not change significantly with interdune
 448 spacing, but the downward flow in the separated-shear layer is faster for more closely-
 449 spaced cases; the maximum vertical velocity for Case 5 is only 56% of the that in Case
 450 1. Turbulent kinetic energy and the Reynolds shear stress are smaller for largely-spaced
 451 dunes (Case 5) since the separated flow has a smaller velocity gradient, $\partial\langle\bar{u}\rangle/\partial y$ (Figure

452 12(a)). The difference in the turbulent kinetic energy (Figure 12(c)) and the Reynolds
453 shear stress (Figure 12(d)) decreases as the profiles move downstream and the effect of
454 the interdune spacing becomes negligible. On the other hand, vertical velocities (Figure
455 12(b)) coincide with each other at $x/H = 10.0$ except for Case 1, where the profile is at
456 the toe of the following dune, and the vertical velocity is directed upwards. In conclusion,
457 large-moderate interdune spacings do not affect the turbulence statistics of the separated-
458 shear layer significantly, and by $10H$ after the crest all statistics converge. However, if
459 the spacing between the dunes is small, here less than 0.34λ , this conclusion is invalid as
460 the flow can develop for less than $10H$ before the next dune is reached.

3.2. Mean-flow three-dimensionality

461 In Figure 13 we show mean streamlines near the bed (released at $y/H = 0.1$ upstream
462 of the dune). The streamlines close to the centerline plane (labeled by number 1) diverge
463 as they rise on the stoss side, separate at the crest, then move towards the bed. Away from
464 the centerline plane, the streamlines (labeled by number 2, Figure 13) diverge toward the
465 horns and separate at the crest, but, once they enter the separation bubble, they meander
466 towards the horns while remaining near the bed. Streamlines far away from the centerline
467 plane (labeled by number 3, Figure 13) diverge toward the horns and never separate.
468 Contours of the velocity magnitude show that streamlines on the bed are accelerated
469 after passing the barchan.

470 The bed shear-stress is strong over the stoss side of dunes close to the crest (Figure
471 14). At the dune toe, the flow diverges from the centerline plane, and the bed stress
472 decreases, as shown in the profile of Figure 9; away from the centerline and along the
473 horns the stress is large, as the flow rises up the stoss side. Figure 14 shows that the

474 separation bubble does not extend all the way along the horns: the separated flow at the
475 crest reattaches on the bed and, due to the three-dimensionality of the separation line, a
476 nodal point of attachment appears away from the symmetry plane (point $p2$, blue bullet in
477 Figure 14). The bed shear-stress is larger downstream of this point: high-momentum fluid
478 that separated at the crest reattaches, increasing the pressure and the stress. Compared
479 to the streamlines around the nodal point of attachment, a saddle point of separation
480 appears downstream of the dune on the symmetry plane (point $p1$, red bullet in Figure
481 14) where the shear stress is small and the near-bed flow converges towards the centerline
482 plane from the sides. The separation bubble contains a large secondary flow, and a few
483 small secondary flow regions, over the lee side of the dune, which cause weak points of
484 separation and attachment. These features close to the bed are often observed in the
485 separation bubble of three-dimensional objects [*Chapman and Yates, 1991; Omidyeganeh*
486 *and Piomelli, 2013*]. All other cases in our simulations present a similar trend; of note,
487 the bed shear-stress does not change significantly with dune spacing (Figure 9 and 16(*a*)).
488 From a series of streamlines over the stoss side of the dune, we note that the separation
489 bubble and the reattached flow converge to a single streamline along the horn and leave
490 the dune from that side, consistent with Figure 13. The observation that barchan dunes
491 lose sediment from the horns [*Hersen et al., 2004; Franklin and Charru, 2011*], is explained
492 by our results.

493 The dune creates two streamwise vortices that induce secondary flow. In Figure 15
494 contours of mean streamwise vorticity and streamlines in the cross planes (i.e., calculated
495 from V and W components of the velocity only) are shown. As the flow near the bed
496 approaches the dune it diverges toward the closest horn. This induces convergence of

497 high-momentum fluid away from the bed towards the centerline plane, which results in
 498 formation of two counter-rotating streamwise vortices aligned with each horn, and with a
 499 diameter close to the flow depth. The strength of these vortices is two orders of magnitude
 500 smaller than the vorticity of the secondary flow within the separation bubble. This pattern
 501 of secondary flow is consistent for all other cases, but the vorticity magnitude decreases
 502 as the interdune spacing increases. This may be due to the periodic boundary conditions,
 503 since each vortex is amplified by the next dune in the array. Note that in the experiments
 504 of *Palmer et al.* [2012] either a single dune or two dunes only were considered. The
 505 streamwise vortices were, therefore, weaker than in the present case, in which an infinite
 506 array of barchans is considered, each dune strengthening the vortices generated upstream.
 507 Since the downwash in the plane of symmetry is weaker, lower streamwise velocity should
 508 be expected in this plane, compared to the simulations, which was observed in Figure
 509 4(*a-c*).

510 We have already observed how the interdune spacing affects turbulent statistics. In
 511 Figure 16, we show the vertical (wall-normal) and spanwise Reynolds stresses along a line
 512 $0.1H$ from the bed, in the middle of the stoss side ($x/H \simeq -5.0$). The bed shear-stress is
 513 not affected significantly by the interdune spacing (Figure 16(*a*)) and over the stoss side of
 514 the dune, $-4.0 \leq z/H \leq 4.0$, the Reynolds stress is smaller due to the divergence of flow
 515 from the centerline plane, shown in Figure 14. $\langle v'v' \rangle / U_\infty^2$ drops over the stoss side while
 516 along the horns it increases significantly; at small interdune spacing (Case 1), due to the
 517 sheltering effect of the upstream dune, the down flow of the fluid is more significant, which
 518 carries turbulence structures to the near-wall region. The spanwise normal Reynolds stress
 519 (Figure 16(*c*)) has a peak on the centerline of the dune and is larger for smaller interdune

520 spacings. In Case 5, when the distance between dunes is large, $\langle w'w' \rangle / U_\infty^2$ is uniform
521 across the channel, indicating that the sheltering effect of the upstream dune has become
522 much weaker. The effect of the stronger turbulent motions on the sediment transport, and
523 of the turbulence structures penetrating into the internal boundary layer, deserve further
524 future study.

525 Budgets of turbulent kinetic energy on the stoss side are shown in Figure 17 for Cases
526 1 and 5. The dune-to-dune interaction, which is strong in Case 1, results in a much
527 thicker layer in which the turbulent kinetic energy transport is important. Two factors
528 contribute to this effect: the shear layer produced by the upstream dune, which overlays
529 the near-bed boundary layer, and the motion induced by the streamwise vortices, which
530 is much stronger in Case 1. The contribution of the shear layer is most significant in the
531 production of TKE and pressure transport, while the footprint of the streamwise vortices
532 is very clear in the dissipation contours. The mean secondary flow also advects wall
533 turbulence away from the dune (Figure 17(c,d)); in Case 1, mean flow advection is also
534 significant in the wake region (Figure 17(d)).

3.3. Instantaneous flow structures

535 Contours of u' on a plane parallel to the bed and close to it are shown in Figure 18
536 for the cases with the largest and smallest interdune spacings, Cases 5 and 1. The flow
537 approaching the dune in Case 5 has the streaky structure characteristics of a smooth open
538 channel, with alternating streaks of low- and high-momentum fluid. Note the predomi-
539 nance of low-speed streaks in the region immediately inboard of the horns, due to the up
540 flow of the streamwise vortices. Flow acceleration over the stoss side of the dune tends
541 to elongate the streaks, consistent with the observations of *Franklin and Charru* [2011],

542 who observed streamwise stripes with regular spacing on the stoss side of their barchan
 543 dune. On the lee side, spanwise-oriented structures are observed between the horns in
 544 the recirculation region. Downstream of reattachment the structures are reorganized and
 545 within a dune length, the low- and high-speed streaks are reformed. Case 1 presents dif-
 546 ferent characteristics; the streaks are shorter and the footprint of the overlying streamwise
 547 vortices is stronger. The magnitude of fluctuations is larger for Case 1; the closely-spaced
 548 dune arrangement enhances the wall turbulence, and would also affect sediment transport
 549 in mobile-bed barchans.

550 Isosurfaces of the second invariant of the velocity-gradient tensor Q ,

$$551 \quad Q = -\frac{1}{2} \frac{\partial \bar{u}_i}{\partial x_j} \frac{\partial \bar{u}_j}{\partial x_i} \quad (5)$$

552 and pressure fluctuations p' are shown for Cases 5 and 1, respectively, in Figures 19 and
 553 20. Q has been shown to be very effective in visualizing small turbulent eddies, while p'
 554 is better at highlighting the larger coherent structures [Dubief and Delcayre, 2000]. The
 555 white circles highlight some turbulent structures. Narrow elongated streamwise structures
 556 are observed over the stoss side of the dune (region 1 in Figure 19(a)); these structures are
 557 longer than the typical wall streaks, as observed before, because of the acceleration of the
 558 flow on the windward slope. Separated spanwise vortices at the crest are identified by both
 559 Q and p' (region 2). These rollers are generated by a Kelvin-Helmholtz instability of the
 560 strong shear layer after separation of flow at the crest and, while convected downstream,
 561 undergo a three-dimensional instability and lose their coherence (region 3); downstream
 562 of the dune, signs of turbulent activity from the wake region of the upstream dune are still
 563 observed. Away from the centerline plane, large coherent structures are rarely observed
 564 (those in region 4 are an example); when they occur, they do so in the outer region of

565 the flow. These structures are convected downstream and away from the centerline plane
566 by the mean secondary flow (Figure 15). Pressure fluctuations identify large but weak
567 structures away from the bed (region 5) that are not observed by the Q criterion. Coherent
568 structures away from the bed most frequently occur outboard of the horns (regions 4 and
569 5), where the up flow of the secondary flow enhances their advection towards the free-
570 surface.

571 For closely spaced dunes (Case 1) the eddies are significantly more coherent (Figure
572 20). Note that the isosurface levels of p' in this Figure are twice as large as those shown
573 in Figure 19. Most of the structures are observed close to the centerline symmetry plane
574 (regions 1 and 2); outside the horns, large scale packets of eddies rarely appear (region
575 3 is an example). Isosurfaces of p' identify the rollers at the crest of dunes (ellipsoid 1
576 in Figure 20(b)), which are bigger, wider and more coherent in Case 1 compared to Case
577 5, due to a larger velocity gradient in the separated-shear layer (Figure 4). For closely-
578 spaced dunes, the coherent structures convected downstream contribute to flow over the
579 stoss side (region 2), and alter the structures close to the bed (Figure 18).

580 The contours of spanwise vorticity fluctuations and streamwise velocity fluctuations
581 (Figure 21) also show the significant influence of interdune spacing on the flow structures.
582 In Case 1, the flow is affected by the bed roughness much further from the bed, up to $5H$,
583 while in Case 5 very few structures are observed above $2H$. In the separated shear layer,
584 small-scale vortices are observed for both cases, but downstream the eddies are confined
585 to the wake region in Case 5, while the separated eddies mix with the upper part of the
586 shear layer in Case 1. The mean turbulent kinetic energy and Reynolds shear stress are
587 more than 20% larger in the separated shear layer of Case 1 than Case 5 (Figure 12(c,d)).

588 Coherent structures approaching the stoss side of the dune in Case 5 are elongated in the
589 streamwise direction, typical of a boundary layer (Figure 21(a)), while in closely-spaced
590 dunes they more resemble a wake structure, with similar scales in streamwise and normal
591 directions (Figure 21(b)). The contribution of these structures to the turbulent kinetic
592 energy is significant, as shown by *Palmer et al.* [2012].

4. Discussion and conclusions

593 The flow over barchan dunes has been studied through a series of numerical simulations
594 of an infinite array of dunes, with variable spacing between dunes in the streamwise
595 direction. The flow has some characteristics in common with that over transverse dunes
596 (deceleration and acceleration of flow over the stoss side, flow separation and formation of a
597 shear layer at the crest, reattachment on the bed and development of an internal boundary
598 layer), but the complex three-dimensional shape of barchans introduces mean secondary
599 flow across the channel and alters turbulence over the stoss side. The current simulations
600 are validated against experiments [*Palmer et al.*, 2012] and provide a comprehensive three-
601 dimensional picture of mean flow characteristics and instantaneous flow structures.

602 Barchan dunes induce the formation of two counter-rotating streamwise vortices along
603 each horn. These vortices direct high-momentum fluid toward the symmetry plane and
604 low-momentum fluid near the bed away from the centerline. In our configuration with
605 barchans aligned in the spanwise direction, and with the periodic boundary condition
606 used, the streamwise vortices become stable.

607 The flow near the bed, upstream of the dune, diverges from the centerline plane, decel-
608 erates and rises on the stoss side of the dune. Flow close to the centerline plane separates
609 at the crest and reattaches, while far from the centerline plane and along the horns flow

610 separation occurs intermittently. The flow in the separation bubble meanders towards
611 the horns and leaves the dune. We note that the flow in the separation bubble may be
612 capable of transporting high concentrations of sediment that will exit the dune from the
613 horns, which explains many observations in field and laboratory measurements indicating
614 that barchans loose sediment downstream via their horns.

615 The characteristics of the separated-shear layer are altered by the interdune spacing;
616 the separation bubble is smaller, the separated-shear layer is stronger, and the bed shear-
617 stress is larger at smaller interdune spacing. The statistics of the shear layer converge
618 at a distance downstream, $x/H = 10.0$, except for Case 1, in which the shear layer
619 responds more strongly to the presence of the downstream dune. The separated flow
620 at the crest reattaches on the bed, except on the symmetry plane, where a weak saddle
621 point of separation appears on the bed. The features of the separation bubble are similar
622 to other three-dimensional dunes; a nodal point of reattachment appears outside the
623 centerline plane where high-momentum fluid reattaches, and the bed shear-stress is larger
624 downstream of this point than at the center of the dune.

625 An internal boundary layer develops downstream of the reattachment region under zero-
626 pressure gradient, for a distance of $35.5H$ in Case 5; the velocity profiles approach the
627 logarithmic law-of-the wall from below and present a small range of logarithmic behavior.
628 The recovery process of the internal boundary layer slows down after approximately $14.5H$,
629 and then the flow decelerates as it approaches the stoss of the downstream dune. The
630 development of the internal boundary layer has the same features in all cases, but the
631 length of the zero-pressure gradient region decreases to $1.8H$ for Case 1; the internal
632 boundary layer is at the beginning of its development at this distance and the mixing

633 of the overlying wake layer with the boundary layer is still significant. At the toe, the
634 streamwise normal Reynolds stress, likely responsible for sustained sediment transport of
635 the retarded flow, decreases at small interdune spacings.

636 Over the stoss side of the dune, the skin friction increases towards the crest, and also
637 increases slightly at smaller interdune spacing. The acceleration of the flow on the stoss
638 side decreases the Reynolds stresses as the flow rises up the dune, but the spanwise and
639 wall-normal Reynolds stresses are significantly higher along the stoss side for Cases 1 and
640 2 (with small interdune spacing) due to the sheltering effect of the overlying wake region
641 advected from the upstream dune. The largest interdune spacing (2.38λ , where λ is the
642 length of the barchan model) presents characteristics similar to those of an isolated dune
643 in the experiment, indicating that at this distance the sheltering effect of the upstream
644 dune is very weak although the mean velocity is not logarithmic yet. Turbulent kinetic
645 energy budgets show the significance of the production and dissipation of turbulence in
646 the separated-shear layer and in the attached shear layer on the bed; over the stoss side,
647 pressure transports energy from the overlying wake layer towards the bed, and contributes
648 more to the energy transport at smaller interdune spacings.

649 The interdune spacing significantly alters the turbulent flow over the stoss side of the
650 downstream dunes; coherent high- and low-speed streaks are shorter but stronger, and the
651 spanwise normal Reynolds stress is larger at smaller interdune spacing, where spanwise-
652 oriented structures are observed near the bed; they carry the signatures of the separated
653 vortices at the crest of the upstream dune. To the sides of the barchans, typical wall
654 turbulence structures are observed, but coherent eddies generated in the separated-shear
655 layer due to Kelvin-Helmholtz instability are dominant. Coherent structures are gener-

656 ated more frequently with smaller interdune spacings; they are advected further from
657 the bed and remain between the horns, while at larger interdune spacing the structures
658 are advected in the spanwise direction with the mean streamwise vortices and reach the
659 outside of the dunes.

660 These results show the complexities introduced to the flow field by dune three-
661 dimensionality and the significant influence of dune spacing at close bedform separations.
662 They also illustrate that models of flow proposed for isolated bedforms require modifica-
663 tion where the flow fields of dunes interact, and that these interactions will modify the
664 intensity and structure of turbulence generated that will then influence the stoss side of
665 the downstream dune. This modulation of dune flow fields will likely be significant in
666 influencing sediment transport and the nature of dune migration [*Endo et al.*, 2004], and
667 suggests that future work should examine these interactions more fully and in cases where
668 the bed is fully mobile.

669 **Acknowledgments.** This research was supported by the Natural Sciences and Engi-
670 neering Research Council (NSERC) under the Discovery Grant program. The authors
671 thank the High Performance Computing Virtual Laboratory (HPCVL), Queen’s Univer-
672 sity site, for computational support. MO acknowledges the partial support of NSERC
673 under the Alexander Graham Bell Canada NSERC Scholarship Program. UP also ac-
674 knowledges the support of the Canada Research Chairs Program.

References

675 Allen, J. (1968), *Current ripples: their relation to patterns of water and sediment motion*,
676 North-Holland Pub. Co.

- 677 Andreotti, B., P. Claudin, and S. Douady (2002), Selection of dune shapes and ve-
678 locities part 1: Dynamics of sand, wind and barchans, *Euro. Phys. J. B*, *28*, doi:
679 10.1140/epjb/e2002-00236-4.
- 680 Armenio, V., and U. Piomelli (2000), A Lagrangian Mixed Subgrid-Scale Model in Gen-
681 eralized Coordinates, *Flow, Turb. Combust.*, *65*, 51–81.
- 682 Baddock, M. C., I. Livingstone, and G. F. S. Wiggs (2007), The geomorphological signif-
683 icance of airflow patterns in transverse dune interdunes, *Geomorphology*, *87*, 322–336.
- 684 Baddock, M. C., G. F. S. Wiggs, and I. Livingstone (2011), A field study of mean and
685 turbulent flow characteristics upwind, over and downwind of barchan dunes, *Earth Surf.*
686 *Proc. Landf.*, *36*, 1435–1448, doi:10.1002/esp.2161.
- 687 Bagnold, R. A. (1941), *The Physics of Blown Sand and Desert Dunes*, Methuen, London.
- 688 Balachandar, R., and V. C. Patel (2005), Velocity measurements in a developed open
689 channel flow in the presence of an upstream perturbation, *J. Hydr. Res.*, *43*(3), 258–
690 266.
- 691 Best, J. L. (2005), The fluid dynamics of river dunes: A review and some future research
692 directions, *J. Geophys. Res.*, *119*(F04S02), 1–21.
- 693 Breed, C. S., M. J. Grolier, and J. F. McCauley (1979), Morphology and distribution
694 of common 'sand' dunes on mars: Comparison with the earth, *J. Geophys. Res.*, *84*,
695 8183–8204.
- 696 Chapman, G. T., and L. A. Yates (1991), Topology of flow separation on three-dimensional
697 bodies, *Appl. Mech. Rev.*, *44*(7), 329–345.
- 698 Charru, F., and E. M. Franklin (2012), Subaqueous barchan dunes in turbulent shear
699 flow. part 2. fluid flow, *J. Fluid Mech.*, *694*, 131–154.

- 700 Choi, H., and P. Moin (2012), Grid-point requirements for large eddy simulation: Chap-
701 man’s estimates revisited, *Phys. Fluids*, 011702, 011,702–1–5.
- 702 Dong, Z., G. Qian, W. Luo, and H. Wang (2007), Simulation of the effects of stoss slope
703 on the lee airflow pattern over a two-dimensional transverse dune, *J. Geophys. Res.*,
704 112(F03019), doi:10.10292006JF000686.
- 705 Dubief, Y., and F. Delcayre (2000), On coherent vortex identification in turbulence, *J.*
706 *Turbul.*, 1, 1–22.
- 707 Endo, N., K. Taniguchi, and A. Katsuki (2004), Observation of the whole process of
708 interaction between barchans by flume experiments, *Geophys. Res. Lett.*, 31, L12,503,
709 doi:10.1029/2004GL020168.
- 710 Ewing, R. C., and G. Kocurek (2010), Aeolian dune interactions and dune-field pattern
711 formation: White sands dune field, new mexico, *Sedimentology*, 57, 1199–1219.
- 712 Fernandez, R., J. Best, and F. Lopez (2006), Mean flow, turbulence structure and bedform
713 superimposition across the ripple-dune transition, *Wat. Resources Res.*, 42(W05406),
714 doi:10.1029/2005WR004330.
- 715 Finkel, H. J. (1959), The barchans of southern peru, *J. Geology*, 67, 614–647.
- 716 Frank, A., and G. Kocurek (1996), Toward a model for airflow on the lee side of aeolian
717 dunes, *Sedimentology*, 43, 451–458.
- 718 Franklin, E. M., and F. Charru (2011), Subaqueous barchan dunes in turbulent shear
719 flow. part 1. dune motion, *J. Fluid Mech.*, 675, 199–222.
- 720 Germano, M., U. Piomelli, P. Moin, and W. H. Cabot (1991), A dynamic subgrid-scale
721 eddy viscosity model, *Phys. Fluids A*, 3, 1760–1765.

- 722 Hardisty, J., and R. J. S. Whitehouse (1988), Effect of bedslope on desert sand transport,
723 *Nature*, *334*, 302.
- 724 Hermann, H. J., J. S. Andrade Jr., V. Schatz, G. Sauermann, and E. J. R. Parteli (2005),
725 Calculation of the separation streamlines of barchans and transverse dunes, *Physica A*,
726 *357*, 44–49, doi:10.1016/j.physa.2005.05.057.
- 727 Hersen, P., K. H. Andersen, H. Elbelrhiti, B. Andreotti, P. Claudin, and S. Douady (2004),
728 Corridors of barchan dunes: Stability and size selection, *Phys. Rev. E*, *69*(011304), 1–12.
- 729 Hesp, P. A., and K. Hastings (1998), Width, height and slope relationships and aerody-
730 namic maintenance of barchans, *Geomorphology*, *22*, 193–204.
- 731 Hirt, C. W., and B. D. Nicholas (1981), Volume of fluid (vof) method for the dynamics
732 of free boundaries, *J. Comput. Phys.*, *39*, 201–225.
- 733 Iversen, J. D., and K. R. Rasmussen (1994), The effect of surface slope on saltation
734 threshold, *Sedimentology*, *41*, 721–728.
- 735 Jackson, P. S., and J. C. R. Hunt (1975), Turbulent wind flow over a low hill, *Quarterly*
736 *J. Royal Meteo. Soc.*, *101*, 929–955.
- 737 Jordan, S. A. (1999), A large-eddy simulation methodology in generalized curvilinear
738 coordinates, *J. Comput. Phys.*, *148*(2), 322–340.
- 739 Kim, J., and P. Moin (1985), Application of a fractional step method to incompressible
740 Navier-Stokes equations, *J. Comput. Phys.*, *59*, 308–323.
- 741 Kocurek, G., R. C. Ewing, and D. Mohrig (2010), How do bedform patterns arise? new
742 views on the role of bedform interactions within a set of boundary conditions, *Earth*
743 *Surf. Proc. Landf.*, *35*, 51–63, doi:10.1002/esp.1913.

- 744 Kroy, K., S. Fischer, and B. Obermayer (2005), The shape of barchan dunes, *J. Phys.*
745 *Condens. Matter*, *17*, S1229–S1235.
- 746 Lancaster, N. (1985), Variations in wind velocity and sand transport rates on the wind-
747 ward flanks of desert sand dunes, *Sedimentology*, *32*, 581–593.
- 748 Lancaster, N. (1995), *Geomorphology of desert dunes*, Routledge, New York.
- 749 Lancaster, N., W. G. Nickling, C. McKenna Neuman, and V. E. Wyatt (1996), Sediment
750 flux and airflow on the stoss slope of a barchan dune, *Geomorphology*, *17*, 55–62.
- 751 Leonard, A. (1974), Energy cascade in large-eddy simulations of turbulent fluid flows,
752 *Adv. Geophys.*, *18A*, 237–248.
- 753 Lettau, K., and H. H. Lettau (1969), Bulk transport of sand by the barchans of la pampa
754 la hoja in southern peru, *Zeitschrift für Geomorphologie*, *13*, 182–195.
- 755 Lima, A. R., G. Sauermann, H. J. Herrmann, and K. Kroy (2002), Modelling a dune field,
756 *Physica A*, *310*, 487–500.
- 757 Livingstone, I., G. F. S. Wiggs, and C. M. Weaver (2007), Geomorphology of desert sand
758 dunes: A review of recent progress, *Earth Sci. Rev.*, *80*, 239–257.
- 759 McCulloch, D. S., and R. J. Janda (1964), Subaqueous river channel barchan dunes, *J.*
760 *Sed. Petrol.*, *34*, 694.
- 761 McKenna Neuman, C., N. Lancaster, and W. G. Nickling (2000), The effect of unsteady
762 winds on sediment transport on the stoss slope of a transverse dune, silver peak, nv,
763 usa, *Sedimentology*, *47*, 211–226.
- 764 McLean, S. R., and J. D. Smith (1986), A model for flow over two-dimensional bed forms,
765 *J. Hydr. Engng*, *112*(4), 300–317.

- 766 Meneveau, C., T. S. Lund, and W. H. Cabot (1996), A Lagrangian dynamic subgrid-scale
767 model of turbulence, *J. Fluid Mech.*, *319*, 353–385.
- 768 Omidyeganeh, M., and U. Piomelli (2011), Large-eddy simulation of two-dimensional
769 dunes in a steady, unidirectional flow, *J. Turbul.*, *12*(42), 1–31.
- 770 Omidyeganeh, M., and U. Piomelli (2013), Large-eddy simulation of three-dimensional
771 dunes in a steady, unidirectional flow. part 1: Turbulence statistics, *J. Fluid Mech.*,
772 *721*, 454–483.
- 773 Palmer, J. A., R. Mejia-Alvarez, J. L. Best, and K. T. Christensen (2012), Particle-image
774 velocimetry measurements of flow over interacting barchan dunes, *Exp. Fluids*, *52*, 809–
775 829.
- 776 Parsons, D. R., G. F. S. Wiggs, I. J. Walker, R. I. Ferguson, and B. G. Garvey (2004a),
777 Numerical modelling of airflow over an idealised transverse dune, *Env. Mod. Soft.*, *19*,
778 153–162, doi:10.1016/S1364-8152(03)00117-8.
- 779 Parsons, D. R., I. J. Walker, and G. F. S. Wiggs (2004b), Numerical modelling of flow
780 structures over idealized transverse aeolian dunes of varying geometry, *Geomorphology*,
781 *59*, 149–164.
- 782 Radhakrishnan, S., U. Piomelli, A. Keating, and A. Silva Lopes (2006), Reynolds-averaged
783 and large-eddy simulations of turbulent non-equilibrium flows, *J. Turbul.*, *7*(63), 1–30.
- 784 Radhakrishnan, S., U. Piomelli, and A. Keating (2008), Wall-modeled large-eddy simula-
785 tions of flows with curvature and mild separation, *ASME J. Fluids Eng.*, *130*(101203).
- 786 Rhie, C. M., and W. L. Chow (1983), Numerical study of the turbulent flow past an airfoil
787 with trailing edge separation, *AIAA J.*, *21*, 1525–1532.
- 788 Schlichting, H. (1955), *Boundary-Layer Theory*, Pergamon Press, New York.

- 789 Silva Lopes, A., and J. M. L. M. Palma (2002), Simulations of isotropic turbulence using
790 a non-orthogonal grid system, *J. Comput. Phys.*, *175*(2), 713–738.
- 791 Silva Lopes, A., U. Piomelli, and J. M. L. M. Palma (2006), Large-eddy simulation of the
792 flow in an S-duct, *J. Turbul.*, *7*(11), 1–24.
- 793 Takahashi, S., M. Du, P. Wu, T. Maki, and S. Kawashima (1998), Three dimensional
794 numerical simulation of the flow over complex terrain with windbreak hedge, *Env. Mod.*
795 *Soft.*, *13*, 257–265.
- 796 Walker, I. J., and W. G. Nickling (2002), Dynamics of secondary airflow and sediment
797 transport over and in the lee of transverse dunes, *Prog. Phys. Geog.*, *26*(1), 47–75.
- 798 Walker, I. J., and W. G. Nickling (2003), Simulation and measurement of surface shear
799 stress over isolated and closely spaced transverse dunes in a wind tunnel, *Earth Surf.*
800 *Proc. Landf.*, *28*, 1111–1124.
- 801 Walmsley, J. L., and A. D. Howard (1985), Application of a boundary-layer model to flow
802 over an aeolian dune, *J. Geophys. Res.*, *90*, 10,631–10,640.
- 803 Weaver, C. M., and G. F. S. Wiggs (2011), Field measurements of mean and turbulent
804 airflow over a barchan sand dune, *Geomorphology*, *128*, 32–41.
- 805 Wiggs, G. F. S., I. Livingstone, and A. Warren (1996), The role of streamline curvature
806 in sand dune dynamics: evidence from field and wind tunnel measurements, *Geomor-*
807 *phology*, *17*, 29–46.
- 808 Wippermann, F. K., and G. Gross (1986), The wind-induced shaping and migration of
809 an isolated dune: a numerical experiment, *Bound.-Lay. Meteorol.*, *36*, 319–334.

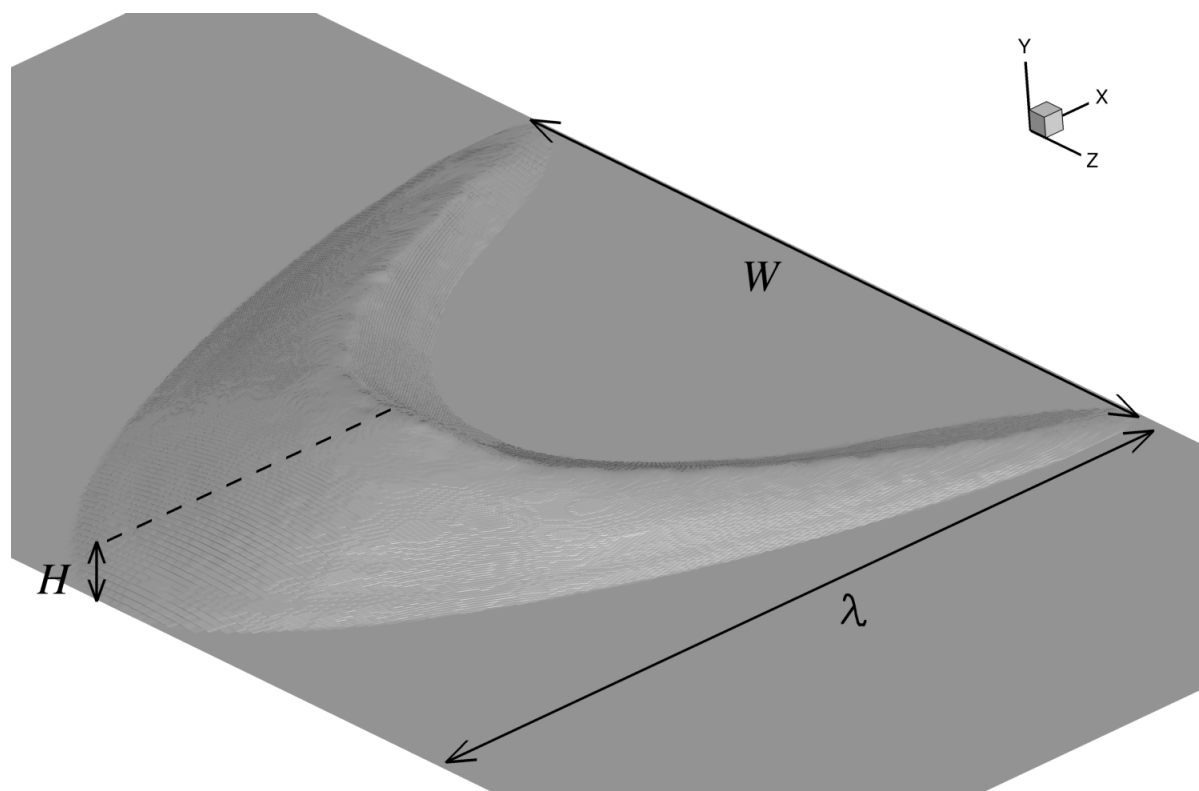


Figure 1. Geometry of the barchan dune model.

Case No.	Spacing	$N_x \times N_y \times N_z$	Δx_{max}^+	Δy_{max}^+	Δz_{max}^+
1	0.00 λ	160 \times 281 \times 512	28.86	0.83	10.55
2	0.34 λ	192 \times 281 \times 512	29.49	0.85	10.78
3	0.68 λ	224 \times 281 \times 512	28.67	0.82	10.48
4	1.02 λ	256 \times 281 \times 512	28.81	0.83	10.53
5	2.38 λ	384 \times 281 \times 512	27.15	0.78	9.92

Table 1. Properties of the test cases. The interdune spacing is defined as the distance between the streamwise location of the horns of upstream dune and the base of the upstream stoss side of the downstream dune.

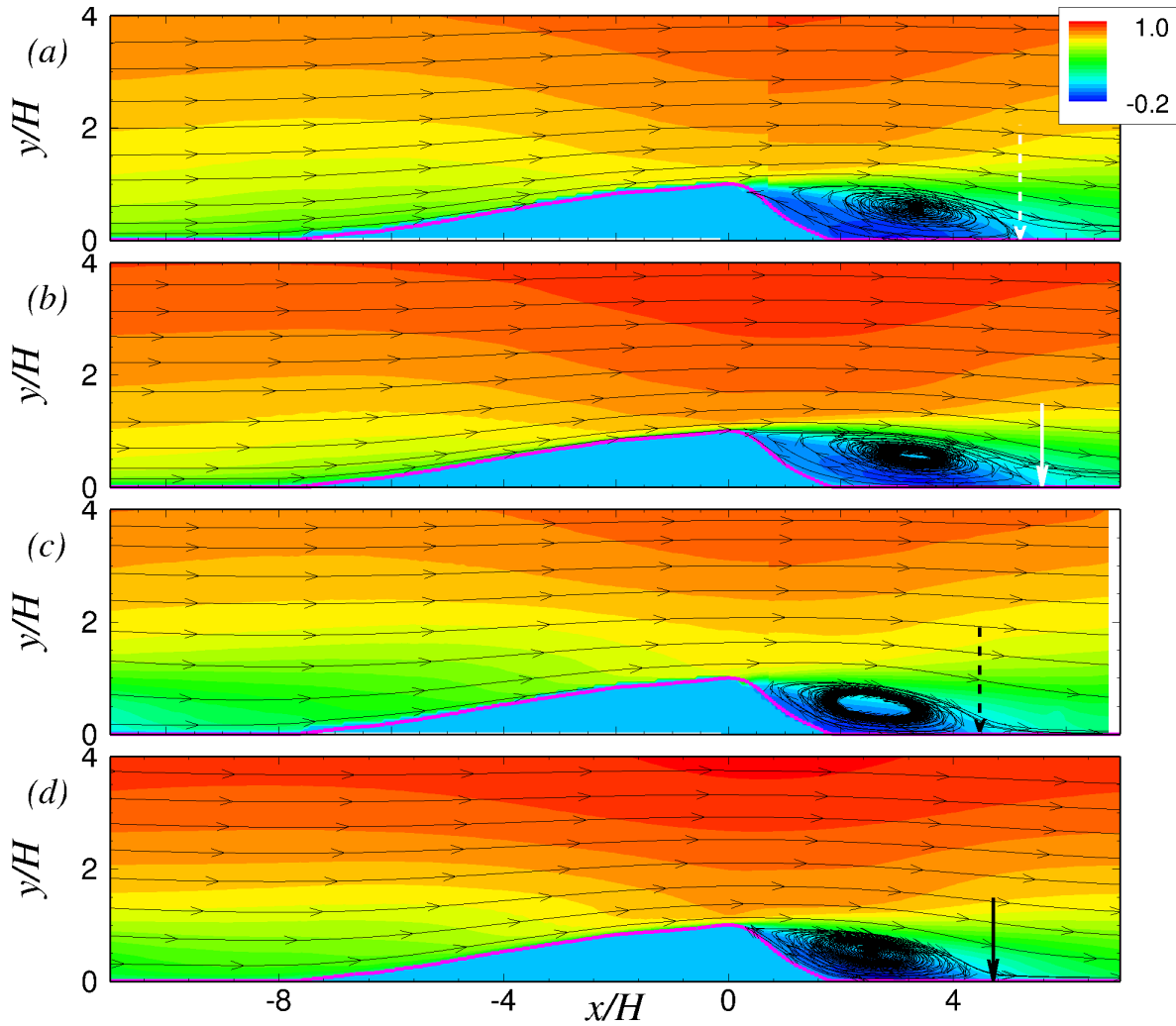


Figure 2. Contours of streamwise velocity, $\langle \bar{u} \rangle / U_\infty$, and streamlines on the centerline plane of (a) isolated dune [Palmer *et al.*, 2012], (b) Case 5, (c) downstream dune of zero interdune-spacing array [Palmer *et al.*, 2012], and (d) Case 1. Arrows show the streamwise position of the reattachment point.

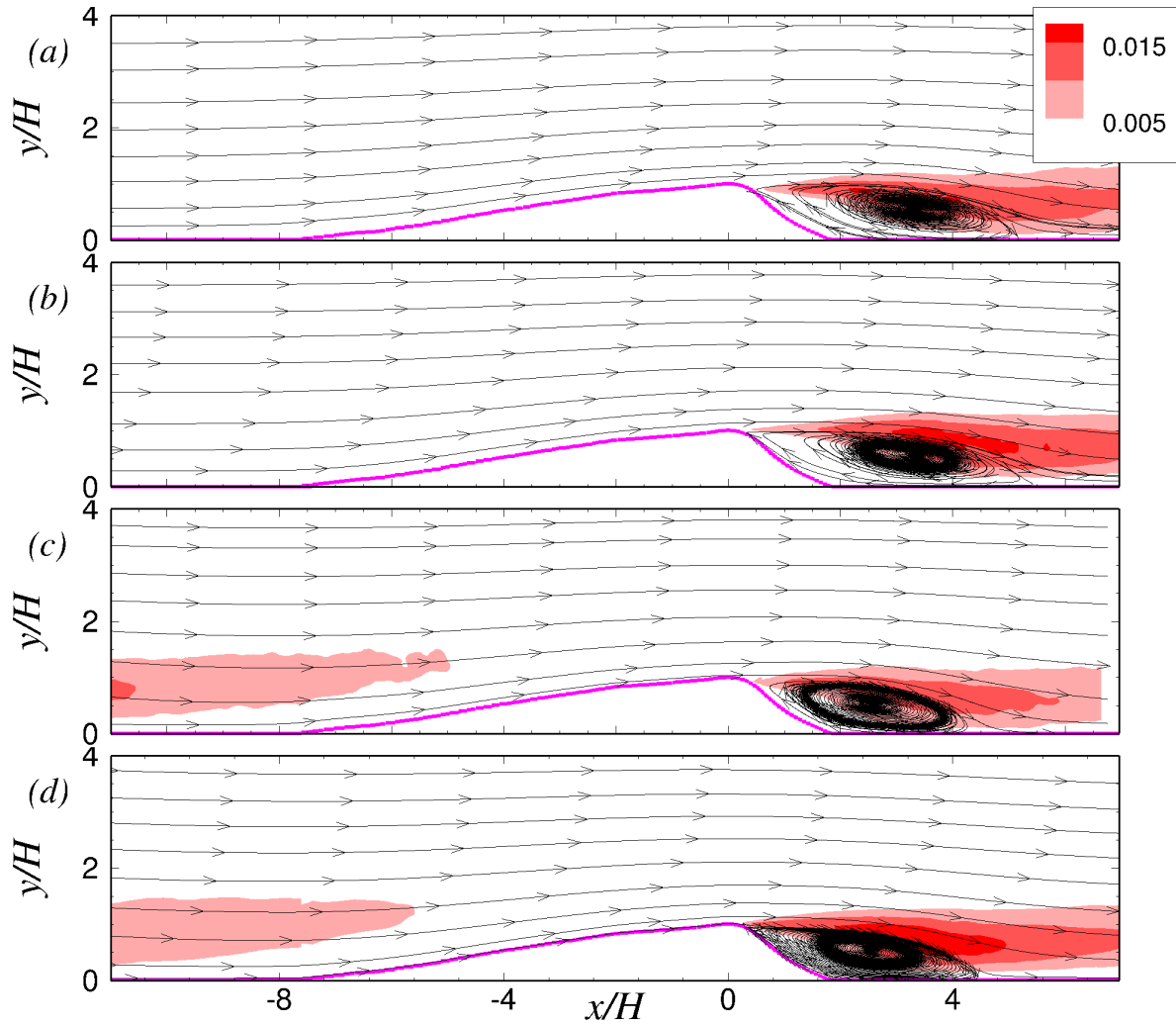


Figure 3. Contours of Reynolds shear stress, $-\langle u'v' \rangle / U_\infty^2$, and streamlines on the centerline plane of (a) isolated dune [Palmer *et al.*, 2012], (b) Case 5, (c) downstream dune of zero interdune-spacing array [Palmer *et al.*, 2012], and (d) Case 1.

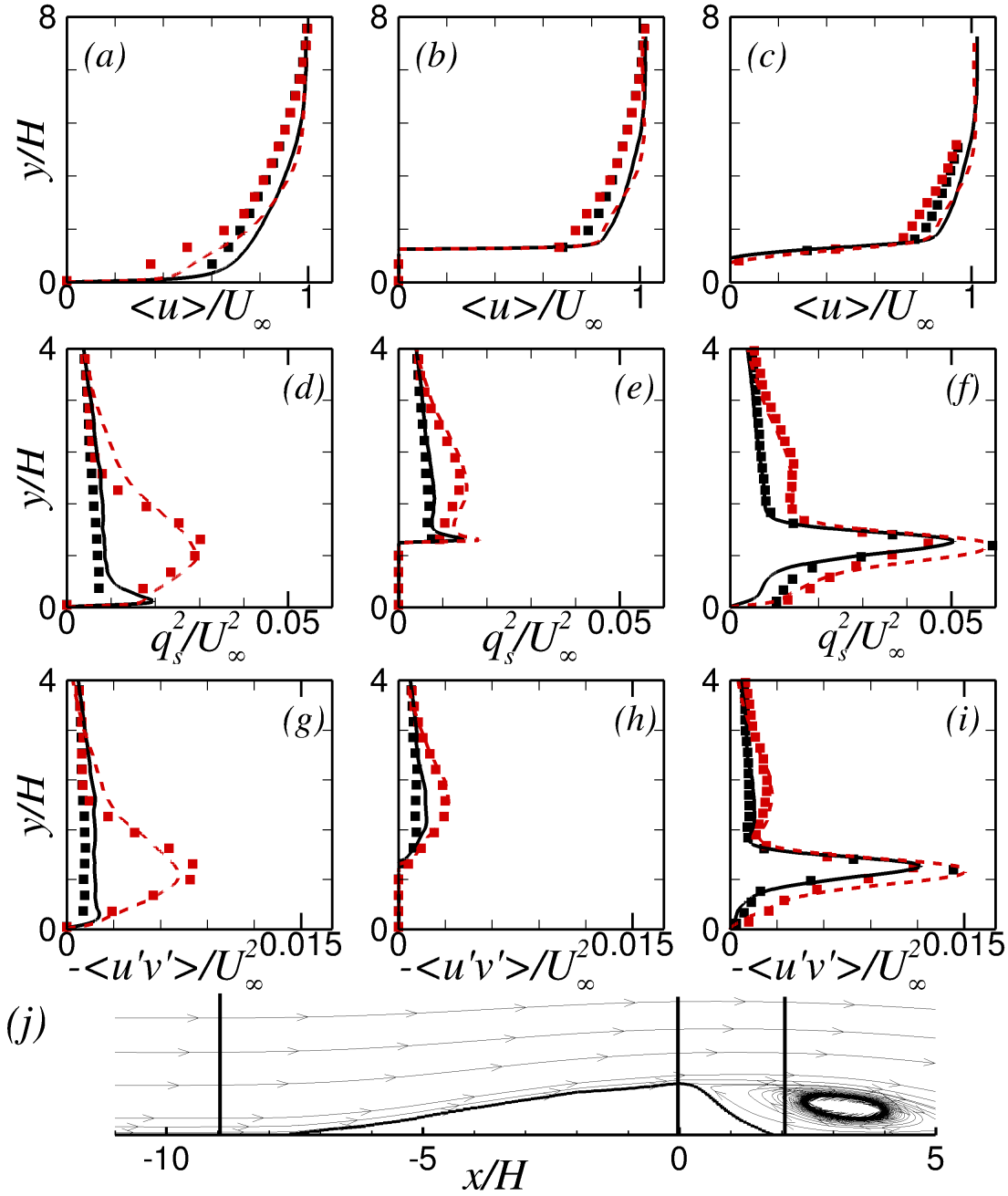


Figure 4. (a-c) Streamwise velocity profiles, (d-f) Planar turbulent kinetic energy, and (g-i) Reynolds shear stress at (a,d,g) $x/H = -9.0$, (b,e,h) $x/H = 0.0$, and (c,f,i) $x/H = 2.0$; — Case 5, - - - Case 1, ■ isolated dune, and ■ zero spacing in the experiment [Palmer *et al.*, 2012].

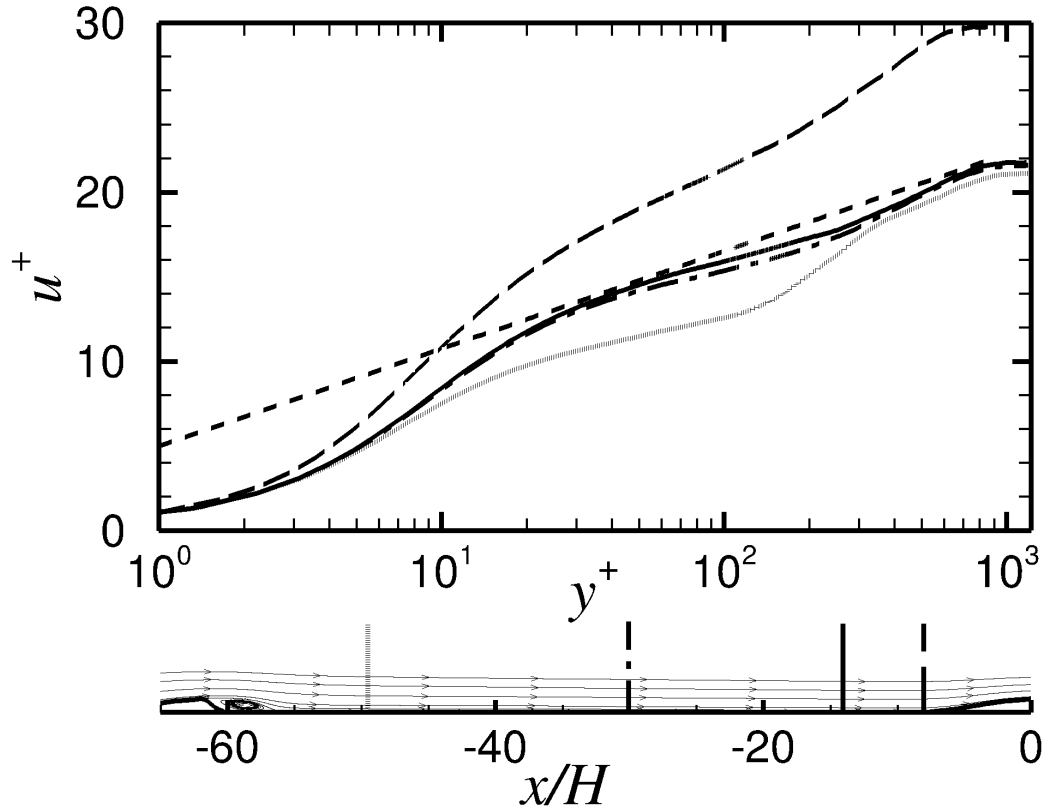


Figure 5. Mean velocity profiles in wall units for Case 5 at the locations shown in (d).

--- Logarithmic law-of-the-wall: $u^+ = \ln y^+ / \kappa + 5.0$.

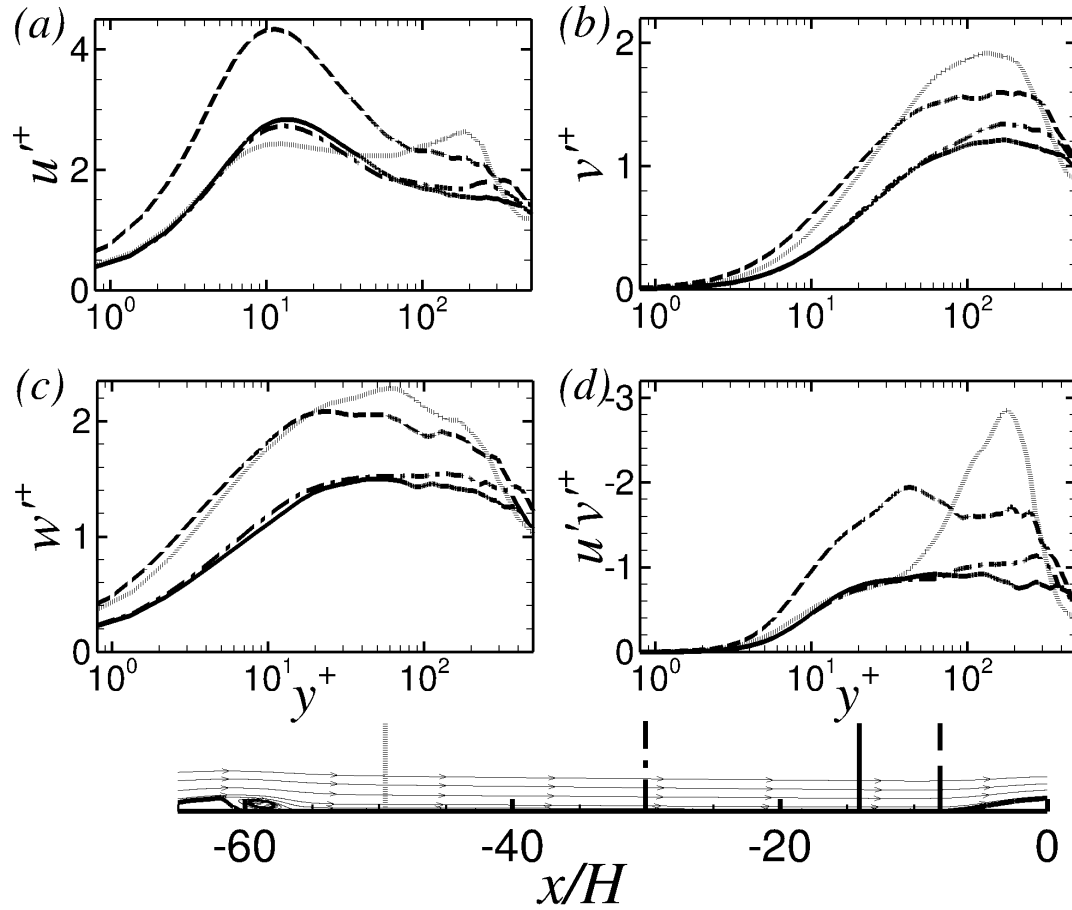


Figure 6. RMS velocity profiles and Reynolds shear stress in wall units for Case 5 at the locations shown in (d); (a) u'_{rms} , (b) v'_{rms} , (c) w'_{rms} , (d) $u'v'^+$.

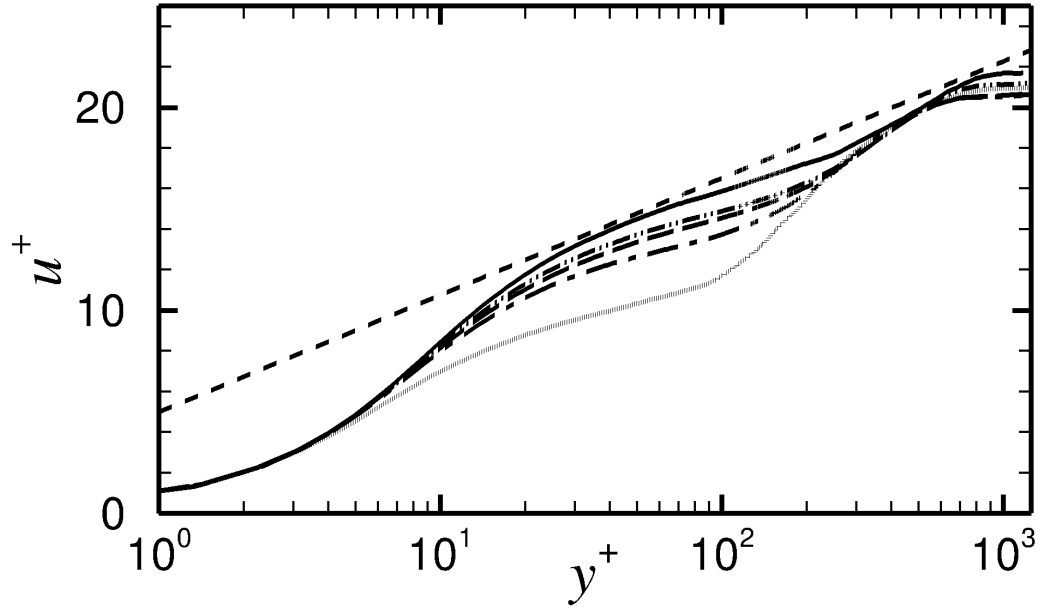


Figure 7. Mean velocity profiles in wall units at the toe of the dune. --- Case 1, $x/H = -9.8$; --- Case 2, $x/H = -11.2$; --- Case 3, $x/H = -12.2$; ---- Case 4, $x/H = -12.8$; — Case 5, $x/H = -14$. --- Logarithmic law-of-the-wall: $u^+ = \ln y^+ / \kappa + 5.0$.

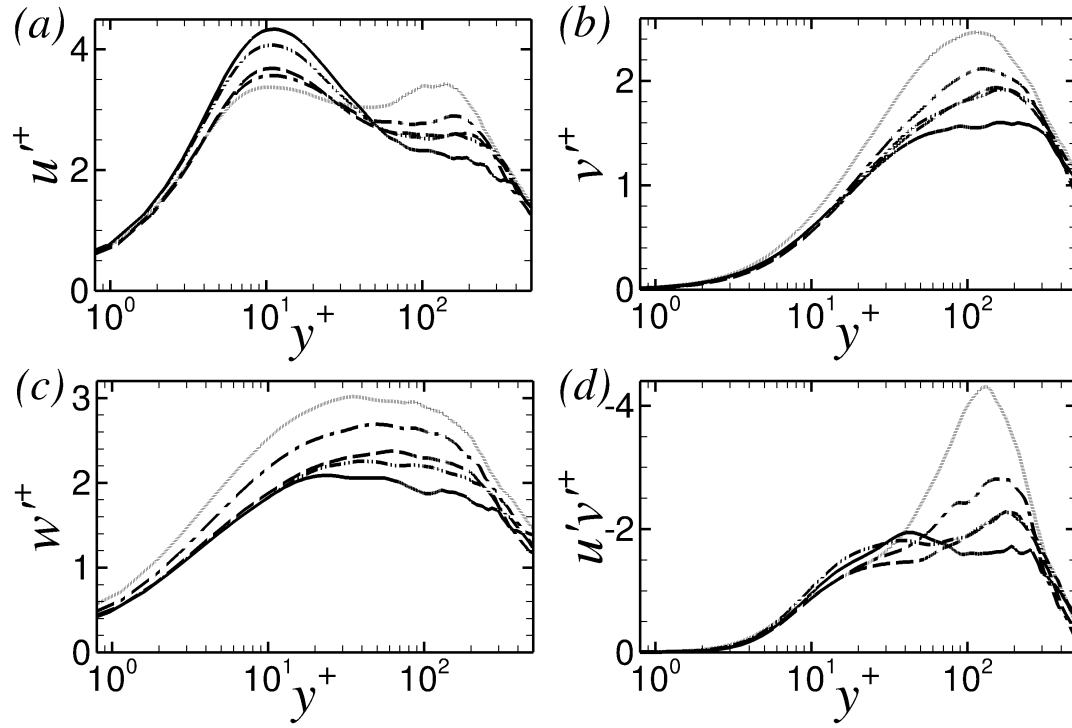


Figure 8. RMS velocity profiles and Reynolds shear stress in wall units at the toe of the dune. --- Case 1, $x/H = -9.8$; --- Case 2, $x/H = -11.2$; --- Case 3, $x/H = -12.2$; ---- Case 4, $x/H = -12.8$; — Case 5, $x/H = -14$.

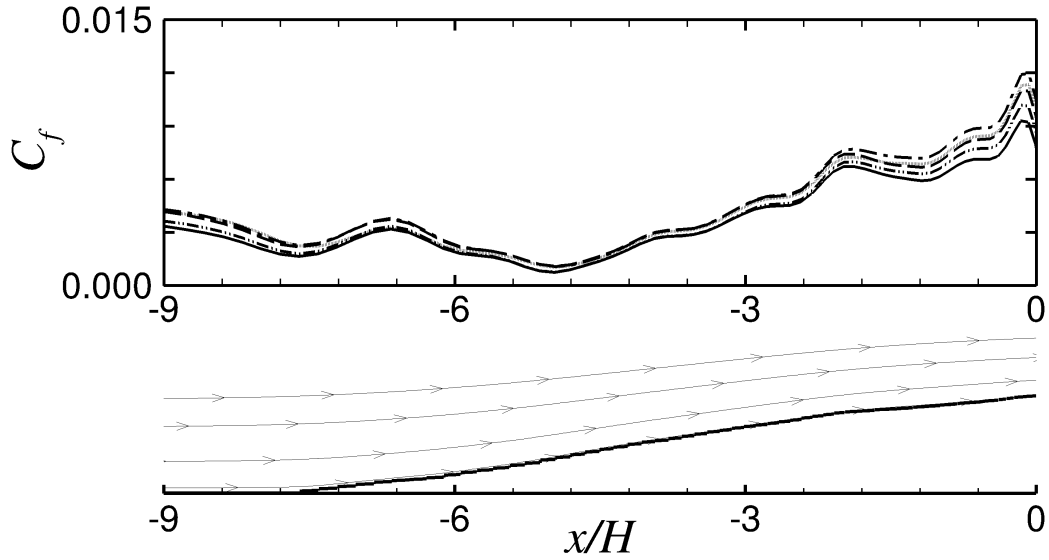


Figure 9. Skin friction coefficient on the stoss side of dunes ($-8.0 \leq x/H \leq 0.0$).

--- Case 1; --- Case 2; -.-.- Case 3; - - - - Case 4; — Case 5.

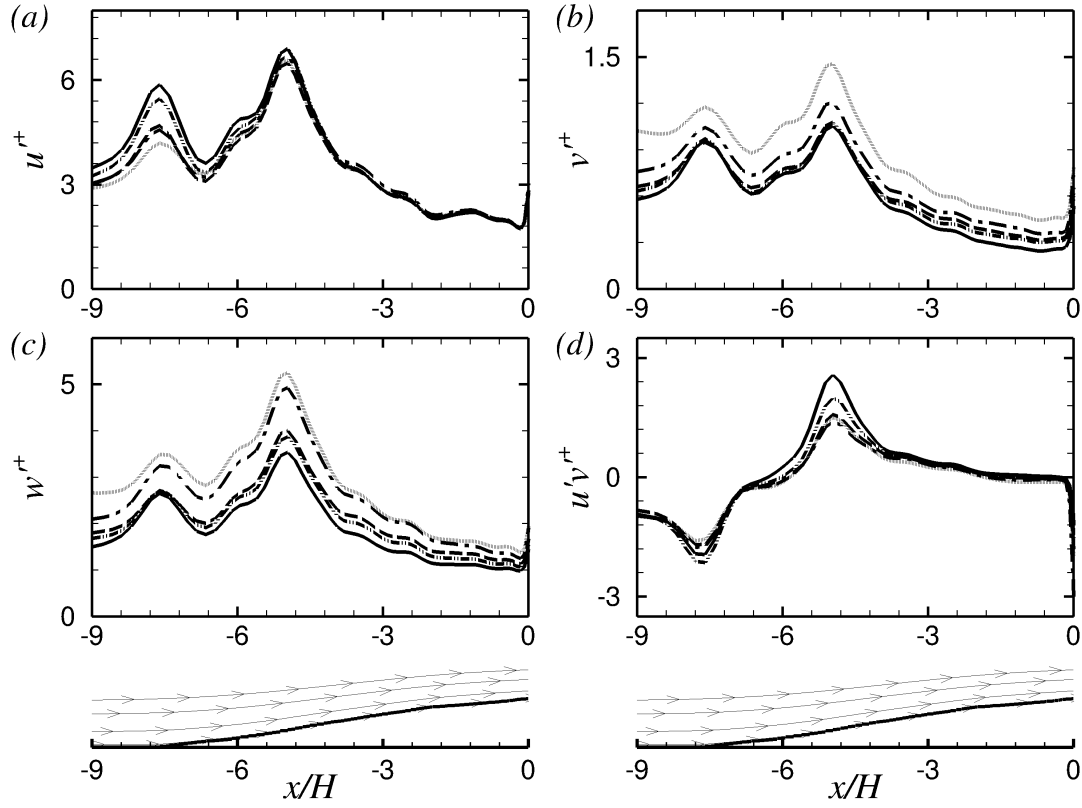


Figure 10. RMS velocity profiles and Reynolds shear stress in wall units; (a) u'_{rms} , (b) v'_{rms} , (c) w'_{rms} , (d) $u'v'^+$ along the stoss side of dunes on the centerline symmetry plane. --- Case 1; --- Case 2; -.-.- Case 3; -.-.- Case 4; — Case 5.

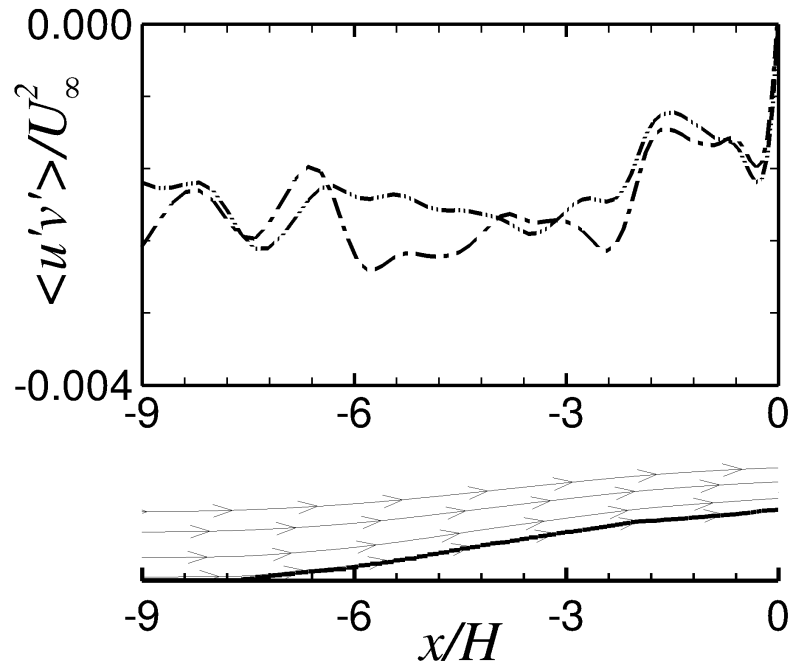


Figure 11. Reynolds shear stress in the parallel- and normal-to-bed coordinate frame along the stoss side of dunes on the centerline symmetry plane. --- Case 2; -.-.- Case 4.

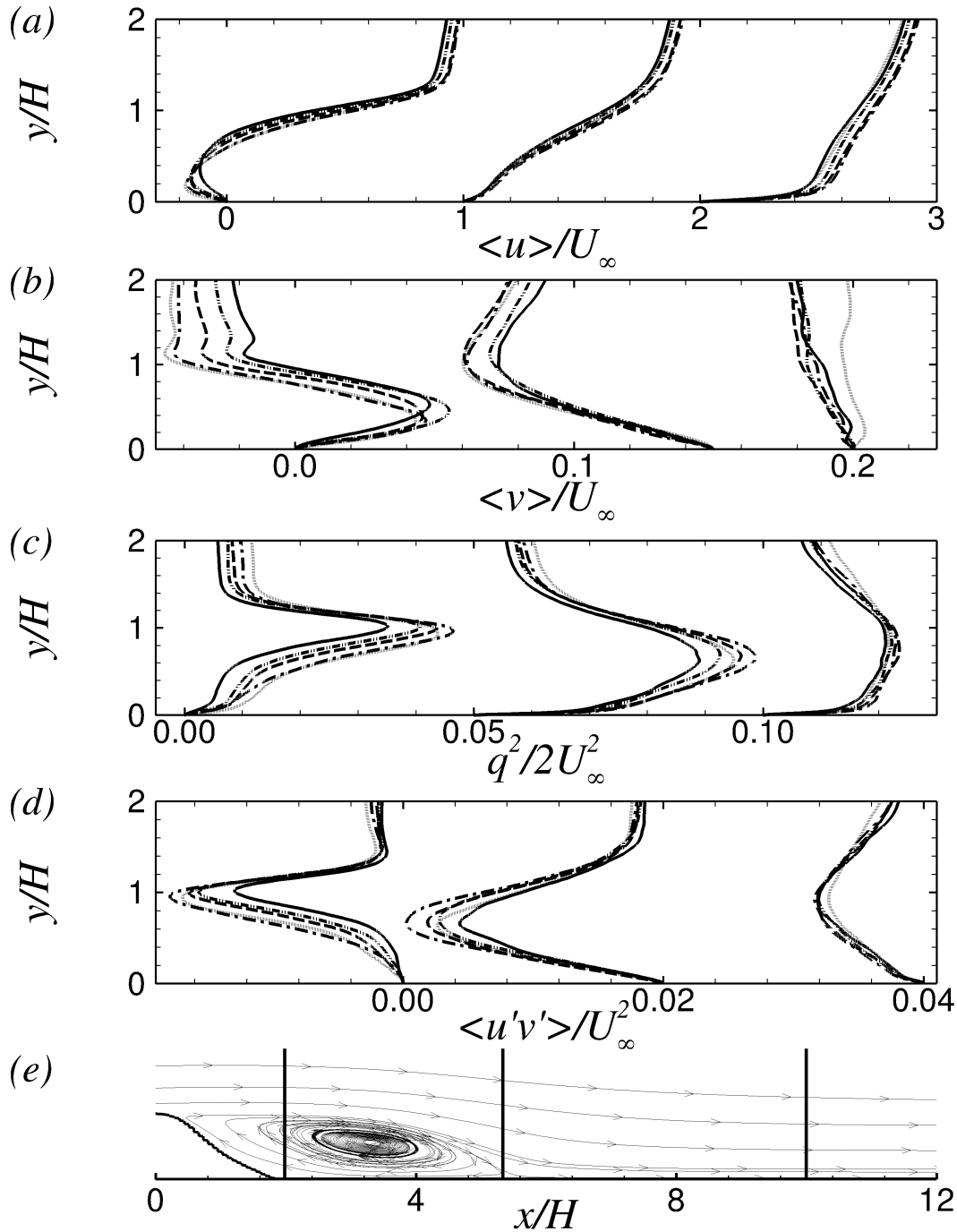


Figure 12. (a) $\langle \bar{u} \rangle / U_\infty$, (b) $\langle \bar{v} \rangle / U_\infty$, (c) $\langle \bar{w} \rangle / U_\infty^2$, and (d) $\langle u'v' \rangle / U_\infty^2$ over three vertical lines at $x/H = 2.0$ passing through the separation zone, $x/H = x_r$ at the reattachment point, and $x/H = 10.0$ downstream of the reattachment point and aligned with the streamwise location of horns. --- Case 1; --- Case 2; - - - Case 3; - - - Case 4; — Case 5.

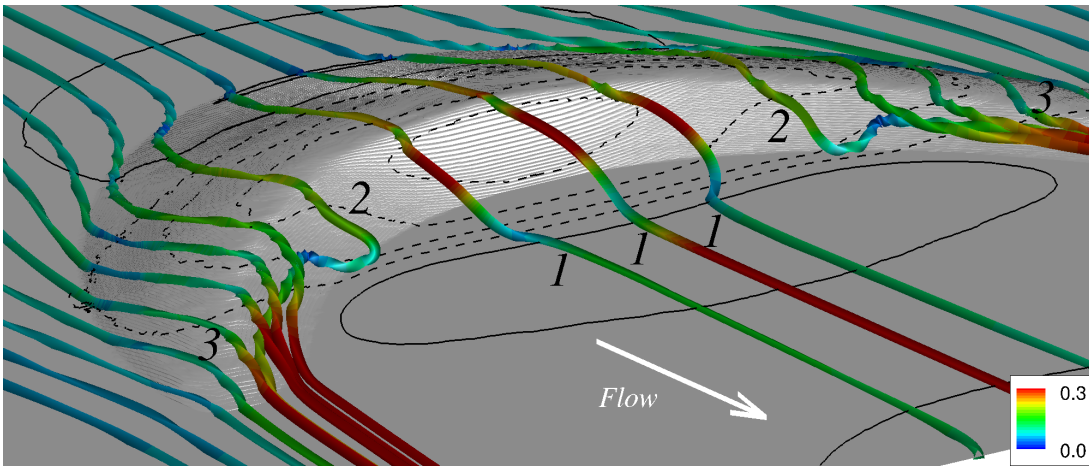


Figure 13. Streamlines close to the bed for the barchan dune of Case 3. Streamlines are colored with the magnitude of the velocity vector. Contour lines of mean pressure are shown on the bed surface; — $\langle \bar{p} \rangle = 0.0$, --- $\langle \bar{p} \rangle = -0.005\rho U_\infty^2$.

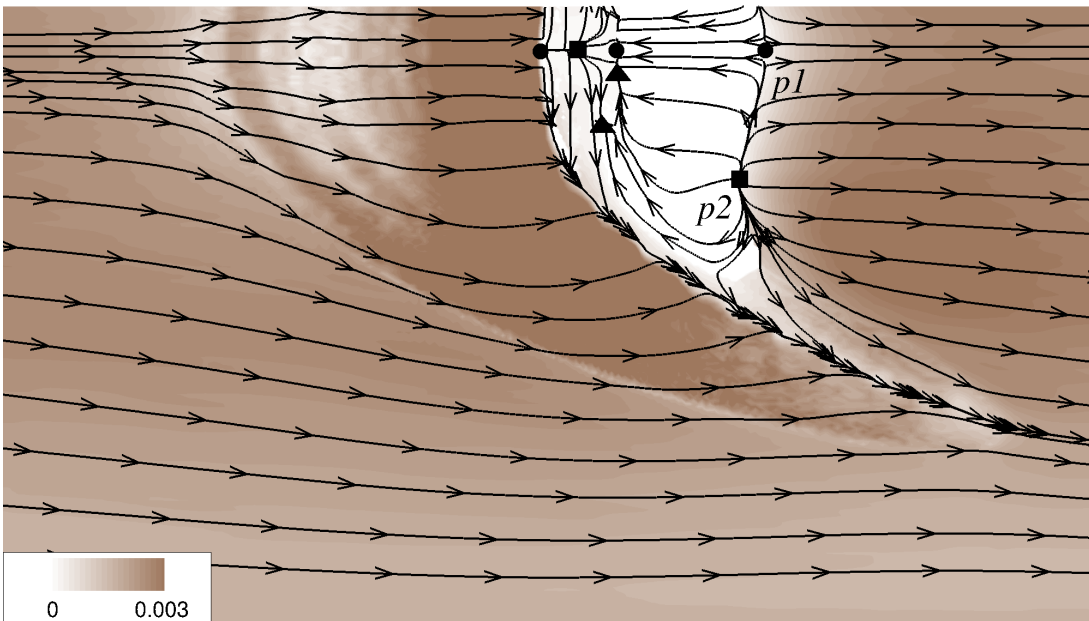


Figure 14. Contours of bed shear-stress, $\tau_w / \rho U_\infty^2$ for Case 3. Streamlines represent the flow direction at the first grid point above the bed surface. ● saddle points of separation; ■ nodal points of attachment; ▲ nodal points of separation

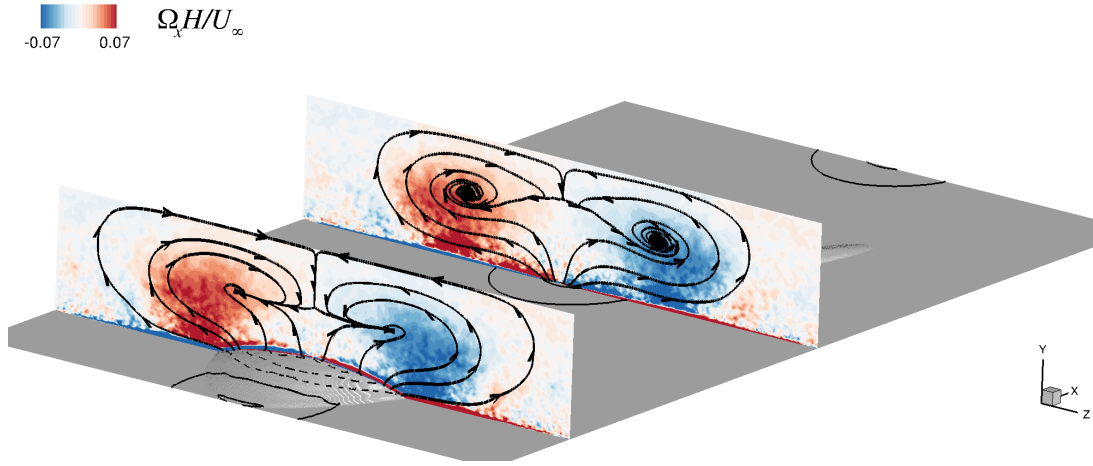


Figure 15. Contours of mean streamwise vorticity, $\Omega_x H/U_\infty$, on two vertical planes across the channel at the crest, $x/H = 0.0$, and at the toe, $x/H = -8.0$, for Case 3. Streamlines tangential to these planes show the secondary flow. Contour lines of the mean pressure are shown on the bed surface; — $\langle \bar{p} \rangle = 0.0$, --- $\langle \bar{p} \rangle = -0.005\rho U_\infty^2$.

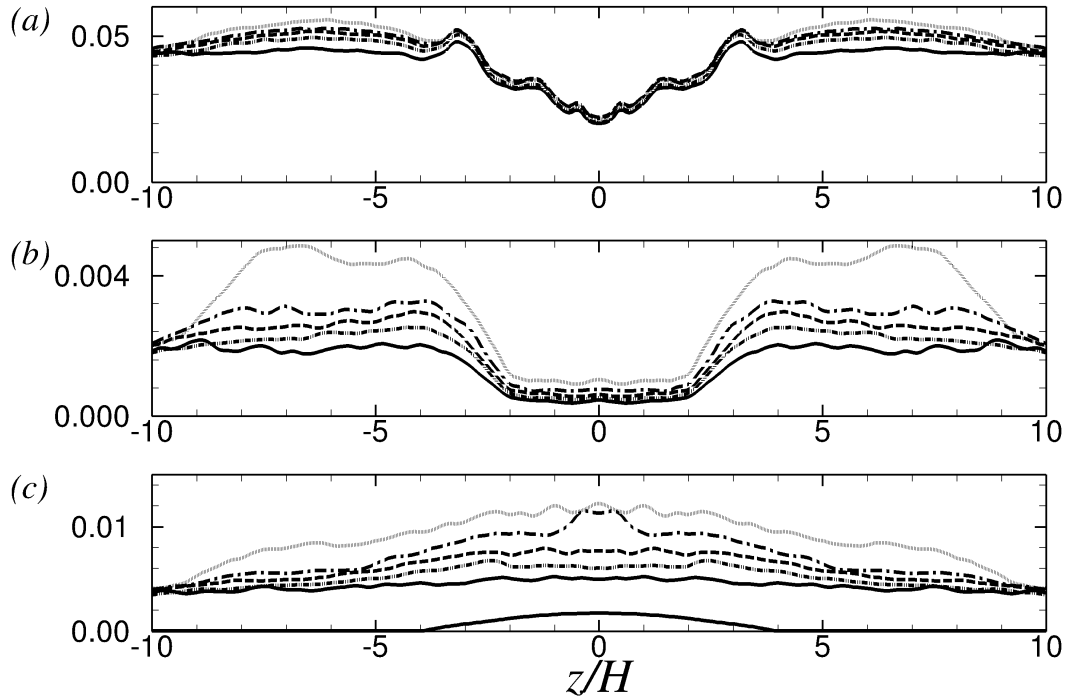


Figure 16. (a) u_τ/U_∞ , (b) $\langle v'v' \rangle / U_\infty^2$, and (c) $\langle w'w' \rangle / U_\infty^2$ on the stoss side ($x/H = -5.0$), $0.1H$ above the bed. --- Case 1; --- Case 2; -.- Case 3; - - - Case 4; — Case 5

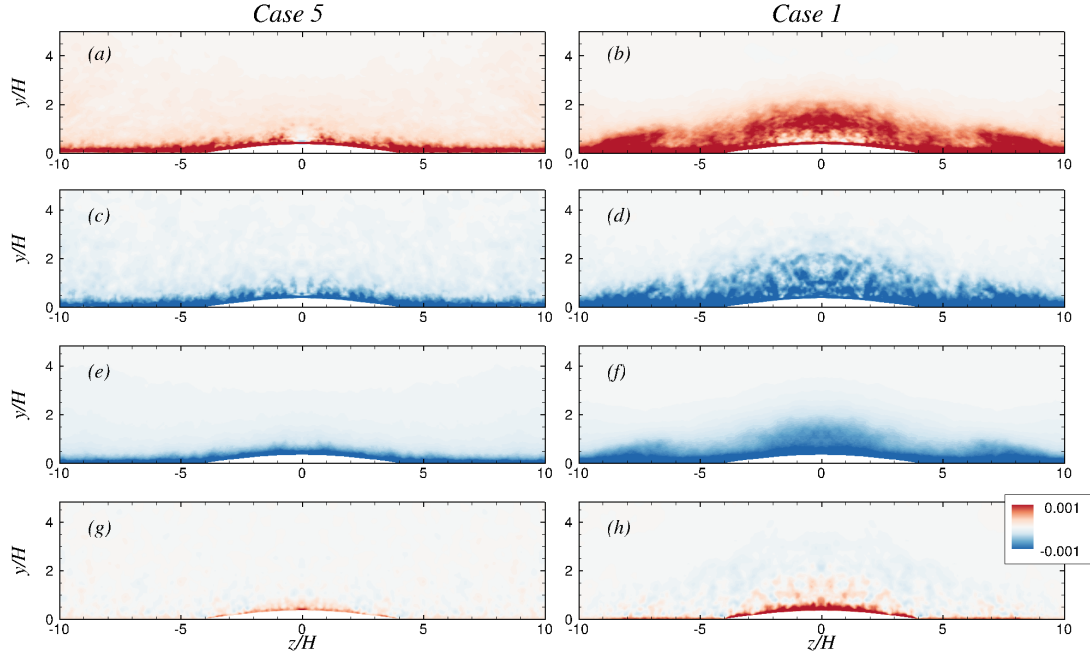


Figure 17. Contours of terms in the turbulent kinetic energy budget at $x/H = -5.0$: (a,b) production, $-\langle u'_i u'_j \rangle \frac{\partial \langle \bar{u}_i \rangle}{\partial x_j}$, (c,d) mean-flow advection, $-\langle \bar{u}_j \rangle \frac{\partial k}{\partial x_j}$, (e,f) dissipation, $-\nu \left\langle \frac{\partial u'_i}{\partial x_j} \frac{\partial u'_i}{\partial x_j} \right\rangle + \left\langle \frac{\partial u'_i}{\partial x_j} \tau'_{ij} \right\rangle$, and (g,h) pressure transport, $-\frac{1}{\rho} \left\langle u'_i \frac{\partial p'}{\partial x_i} \right\rangle$. (a,c,e,g) Case 5, and (b,d,f,h) Case 1.

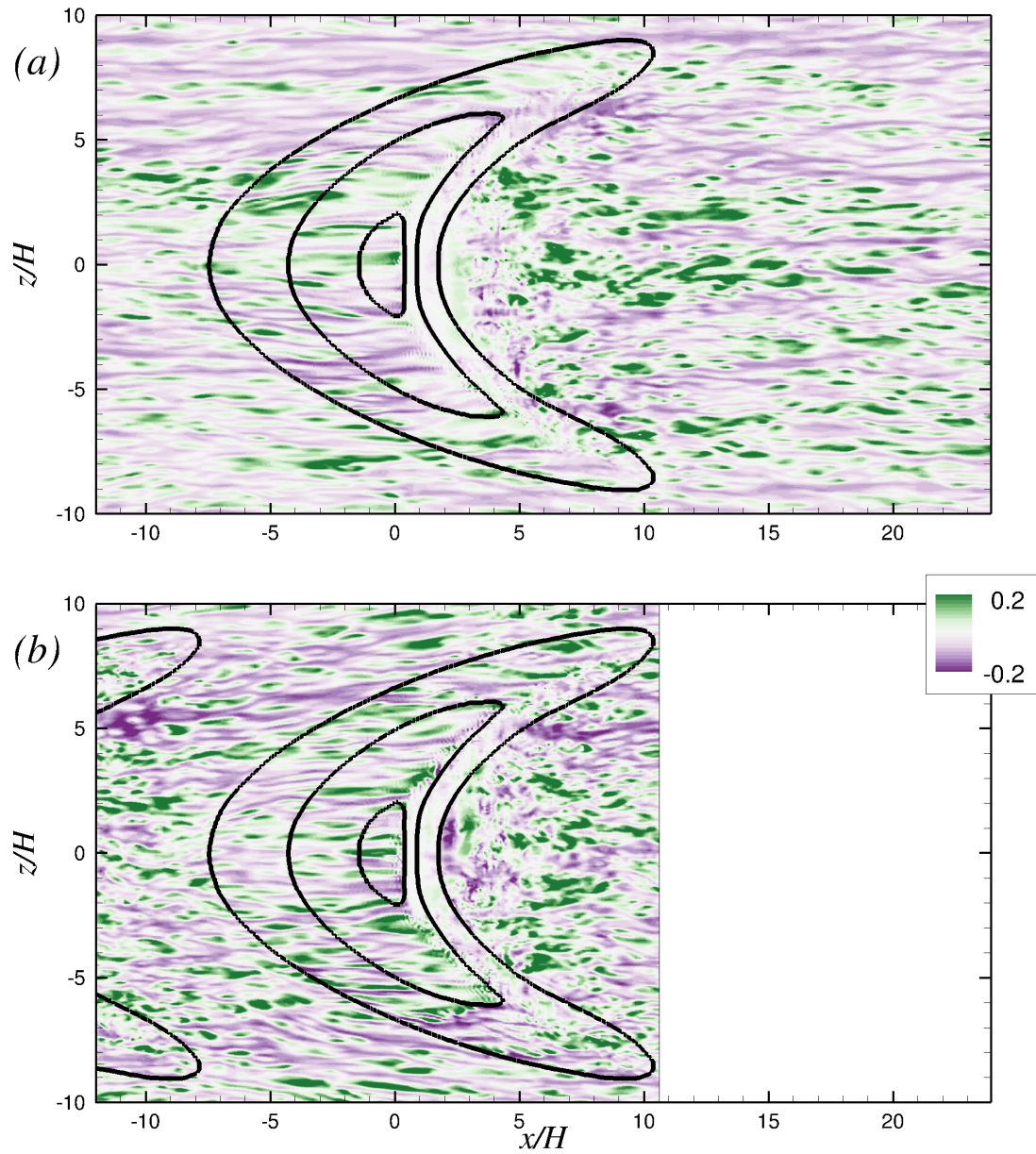


Figure 18. Contours of u' on a plane parallel to the bed surface with a distance $0.025H$ for (a) Case 5, and (b) Case 1. The lines correspond to the bed levels at $y/H = 0.03$, 0.5 , and 0.9 .

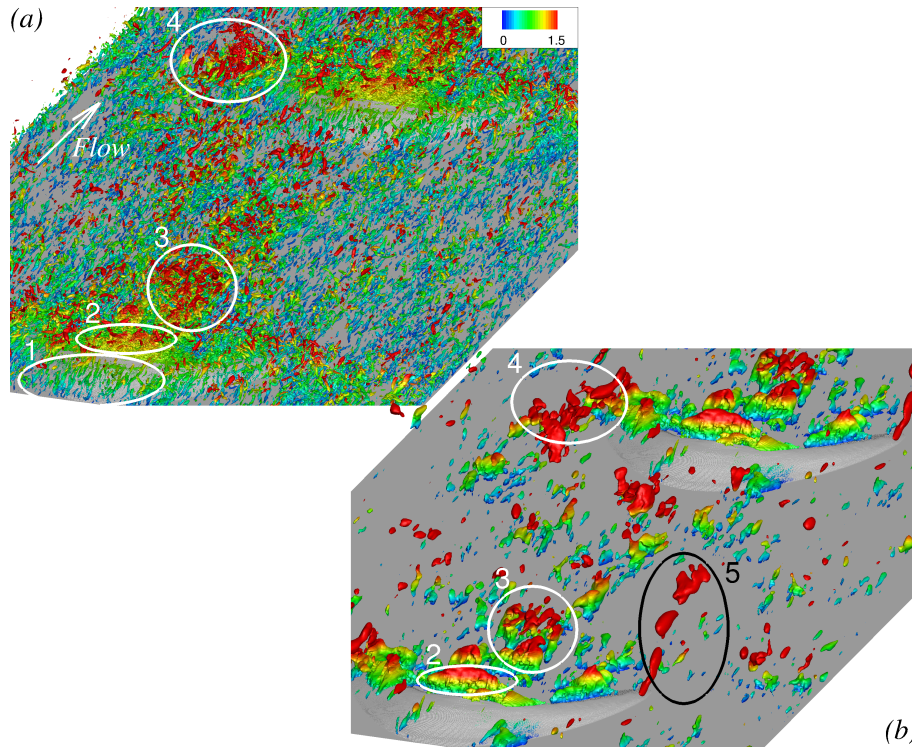


Figure 19. (a) Isosurfaces of the second invariant of velocity gradient tensor, $QH^2/U_\infty^2 = 0.35$, and (b) isosurfaces of pressure fluctuation, $p'/\rho U_\infty^2 = -0.007$, colored by distance from the bed at $y/H = 0.0$ for Case 5.

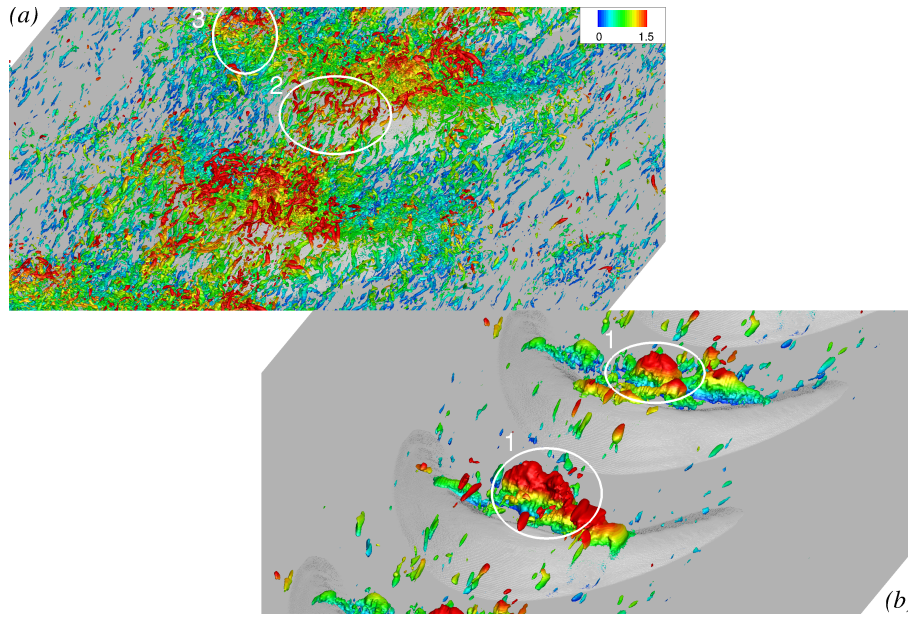


Figure 20. (a) Isosurfaces of the second invariant of velocity gradient tensor, $QH^2/U_\infty^2 = 0.70$, and (b) isosurfaces of pressure fluctuation, $p'/\rho U_\infty^2 = -0.014$, colored by distance from the bed at $y/H = 0.0$ for Case 1.

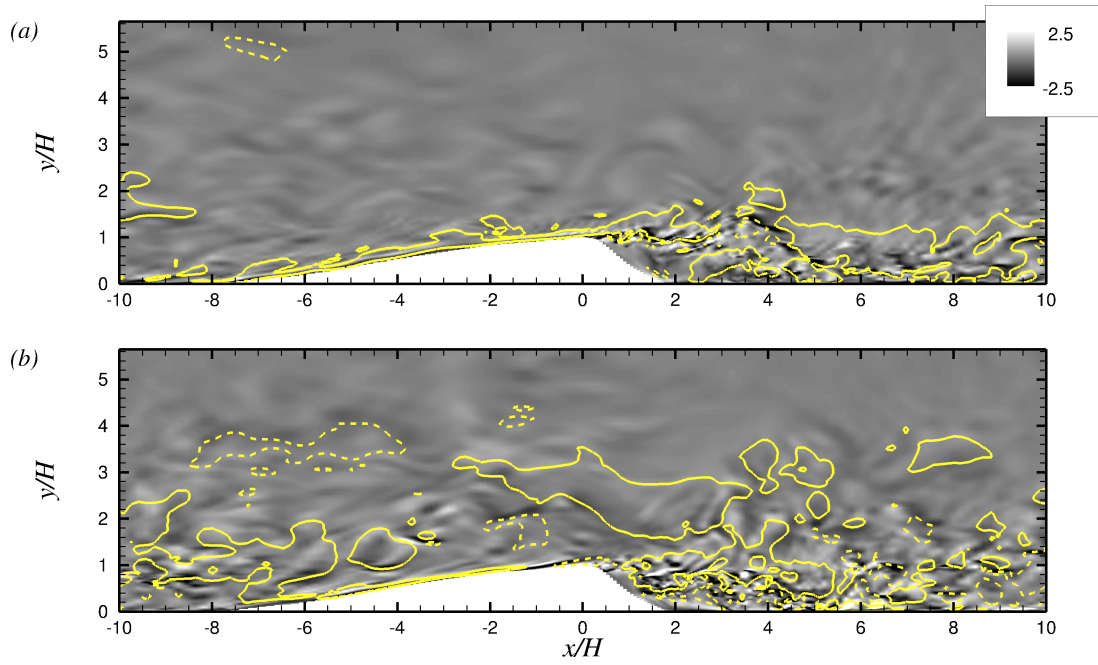


Figure 21. Contours of spanwise vorticity fluctuations, $\omega'_z H/U_\infty$ on the centerline symmetry plane of (a) Case 5 and (b) Case 1. Solid lines represent $u'/U_\infty = 0.12$, and dashed lines show $u'/U_\infty = -0.12$.